Sharp waves, bursts, and coherence: Activity in a songbird vocal circuit is influenced by behavioral state

Abbreviated title: Pallial-striatal dynamics and behavioral state

Author Names and affiliations: Corinna Lorenz[1,2]*, Anindita Das[2]*, Eduarda Gervini Zampieri Centeno[3,5], Hamed Yeganegi[4,6], Robin Duvoisin[1], Roman Ursu[3], Aude Retailleau[3], Nicolas Giret[2], Arthur Leblois[3], Richard H. R. Hahnloser[1], and Janie M. Ondracek[4†]

[1] Institute of Neuroinformatics, University of Zurich and ETH Zurich, 8057, Zurich, Switzerland
[2] Institut des Neurosciences Paris-Saclay, CNRS, 151 route de la rotonde, 91400 Saclay, France
[3] Bordeaux Neurocampus, Institut des Maladies Neurodégénératives, 146 rue Léo-Saignat - 33076 Bordeaux Cedex
[4] Technical University of Munich, TUM School of Life Sciences, Chair of Zoology, Liesel-Beckmann-Straße 4, 85354 Freising, Germany
[5] Amsterdam UMC location Vrije Universiteit Amsterdam, Anatomy and Neurosciences, De Boelelaan 1117, Amsterdam, The Netherlands
[6] Graduate School of Systemic Neurosciences, Ludwig-Maximilians-University Munich, Großhaderner Str. 2, 82152, Planegg, Germany
(*) Authors contributed equally
([†]) Corresponding author

Corresponding author email address: janie.ondracek@tum.de

Acknowledgements: This research was supported by the Agence Nationale de la Recherche (SleepinBrainDyn) and the CNRS (International Emerging Action, project BirdSleep) to AD; the EUR NEURO (EUR/7410-5) and Bordeaux Neurocampus - GPR BRAIN 2030 (GP/7200R-12) to EGZC; the Deutsche Forschungsgemeinschaft (ON 151/1-1) and the Daimler und Benz Stiftung (PN 32-09/18) to JMO; the BayFrance program (FK23 2019) to CL, HY, NG, and JMO. The authors would further like to thank and acknowledge Melanie Dumont for excellent animal caretaking and Manon Rolland for help with experiments.

Abstract

Similar to motor skill learning in mammals, vocal learning in songbirds requires a set of interconnected brain areas that make up an analogous basal ganglia-thalamocortical circuit known as the anterior forebrain pathway (AFP). Although neural activity in the AFP has been extensively investigated during awake singing, very little is known about its neural activity patterns during other behavioral states. Here, we used chronically implanted Neuropixels probes to investigate spontaneous neural activity in the AFP during natural sleep and awake

periods in male zebra finches. We found that during sleep, neuron populations in the pallial region LMAN (lateral magnocellular nucleus of the nidopallium) spontaneously exhibited synchronized bursts that were characterized by a negative sharp deflection in the local field potential (LFP) and a transient increase in gamma power. LMAN population bursts occurred primarily during non-rapid eye movement (NREM) sleep and were highly reminiscent of sharp-wave ripple (SWR) activity observed in rodent hippocampus. We also examined the functional connectivity within the AFP by calculating the pairwise LFP coherence. As expected, delta and theta band coherence within LMAN and Area X was higher during sleep compared to awake periods. Contrary to our expectations, we did not observe strong coherence between LMAN and Area X during sleep, suggesting that the input from LMAN into Area X is spatially restricted. Overall, these results provide the first description of spontaneous neural dynamics within the AFP across behavioral states.

Significance statement

Although cortical and basal ganglia circuits are known to be required for learning in both mammals and birds, little is known about the ongoing spontaneous activity patterns within these circuits, or how they are modulated by behavioral state. Here we prove the first description of cortical-basal ganglia network activity during sleep and awake periods in birds. Within the pallial area LMAN, we observed population-wide bursting events that were highly reminiscent of hippocampal sharp-wave ripple (SWR) activity, suggesting that large-scale population events have diverse functions across vertebrates.

Introduction

During vocal learning, a juvenile bird transitions from acoustically simple, highly variable “subsongs” to complex and stereotypical adult songs through a process of motor learning (Kollmorgen et al., 2020; Konishi, 1965, 1970; McCasland & Konishi, 1981). Critically involved in this learning process is a set of interconnected brain areas that make up a basal

ganglia-thalamocortical circuit (Fig. 1A) known as the AFP (Andalman & Fee, 2009; Bottjer et al., 1984; Brainard & Doupe, 2000; Farries & Perkel, 2002; Scharff & Nottebohm, 1991)

Within the AFP, the pallial structure LMAN exerts a direct influence on vocal output through its projection to premotor area RA (robust nucleus of the arcopallium), presumably modulating downstream neural activity through bursts of spikes (Kao et al., 2008; Kojima et al., 2013; Palmer et al., 2021). Through this influence, LMAN drives behavioral variability that can be used for learning (Tumer & Brainard, 2007). Area X, part of the avian striatum (Person et al., 2008; Pfenning et al., 2014), is thought to receive an efference copy of activity in LMAN (Andalman & Fee, 2009; Vates et al., 1997; Vates & Nottebohm, 1995), thus placing Area X in a position to evaluate LMAN exploratory activity in the context of the ongoing song via a dopaminergic reward signal (Duffy et al., 2022; Gadagkar et al., 2016).

Many studies have shown that cortical and basal ganglia (BG) circuits are required for learning in both birds (Ali et al., 2013; Andalman & Fee, 2009; Bottjer et al., 1984; Olveczky et al., 2005; Scharff & Nottebohm, 1991; Tumer & Brainard, 2007; Zai et al., 2020) and mammals (Kawai et al., 2015; Lemke et al., 2021; Santos et al., 2015), including humans (Debas et al., 2014). However, relatively little is known about the ongoing spontaneous activity within the basal ganglia-thalamocortical circuit, or how it is modulated by behavioral state.

Indeed, most of what is known about neural activity in AFP has been studied in the context of awake singing. Neurons in LMAN neurons are activated during singing, and neural activity in LMAN changes as a function of social context: spiking signals become more stereotyped during “directed singing” and more variable during “undirected” singing (Kao et al., 2008; Stepanek & Doupe, 2010). Similar to LMAN, neurons in Area X also exhibit contextual spiking responses during singing (Hessler & Doupe, 1999), with bursts of neural activity aligning to specific times within a song motif.

Although the importance of social context has been demonstrated for neurons in LMAN and Area X, very little is known about the ongoing spontaneous activity in these brain regions. How does brain state affect neural activity in LMAN or Area X? How do the spiking activity patterns align to ongoing field oscillations? With the exception of one study that characterized the presence of high gamma oscillations in Area X during sleep (Yanagihara & Hessler, 2012), spontaneous neural activity patterns in the AFP - and how they may be modulated by brain state - remain largely unexplored.

We used a new approach (Lorenz, 2024) to chronically implant Neuropixels1.0 probes (Jun et al., 2017) in order to investigate neural activity in the pallial-striatal network of the AFP during periods of natural sleep and awake behavior in seven male zebra finches. By characterizing spontaneous neural spiking activity in relation to ongoing LFP oscillations in this avian pallial-striatal circuit, we gain insight into the different regimes of neural activity that are present within this circuit across different behavioral states, and which helps inform further studies of the analogous corticostriatal network in mammals.

Materials and Methods

Subjects

Seven male zebra finches (*Taeniopygia guttata*) were used in this study; data were pooled across two laboratories in France (the Neuroscience Paris-Saclay Institute and the Bordeaux Neurocampus). The age of the animals ranged from 76 days post-hatch (dph) to 232 dph at the time of recording. Where it was possible in the figures, we have identified the 3 youngest sub-adult animals (ZF-1, ZF-5, and ZF-7) with pink shading of their names. All animals were bred and housed in the animal facilities of the laboratories. During the experiment, animals

118 were housed individually with water and food *ad libitum* under a 14:10 hr light/dark cycle.
119 Details about the individual animals can be found in Table 1.
120 All experimental procedures were approved by the French Ministry of Research and the
121 ethical committee “Paris-Sud et Centre" (CEEA No. 59, project 2017-25) and “Poissons
122 Oiseaux Nouvelle Aquitaine” (CEEA No. 73, project S73) and performed under the license
123 2015-25 and APAFIS#13413-2018020713145795.

124 Surgery and experiments

125 Chronic Neuropixels implantation surgery

126 The day of the surgery, food and water sources were removed from the cage approximately
127 30 minutes before the start of the surgery. Animals were anesthetized with isoflurane (0.6-
128 1.5% inhalation) and placed in the stereotactic apparatus once the toe flexion reflex was no
129 longer observed. Feathers were removed from the scalp and the area was disinfected with
130 ethanol and betadine. 0.05 microliters of diluted lidocaine (0.5mg/kg) was administered
131 subcutaneously to the scalp and a local anesthetic (0.5 g Emla® creme) was applied to the
132 exposed skin. The scalp was resected and the exposed skull was prepared for the implant
133 by drilling several small holes in the outer bone layer. A small craniotomy contralateral to the
134 final implant was made to place a silver wire in contact with the dura that served as the
135 electrical ground.
136
137 The main craniotomy was made on the right hemisphere at approximately 1.7 mm lateral to
138 the superior sagittal sinus and 4.5 mm anterior to lambda, the confluence of sinuses, with
139 the flat part of the anterior skull rotated to a 50-degree angle. The positions of LMAN and
140 Area X were mapped with high-impedance single-electrodes in order to identify the brain
141 areas based on the firing rate properties thereof.
142

143 A Neuropixels probe version 1.0 (Jun et al., 2017) was implanted 4 to 5 mm deep to
144 penetrate the estimated center of LMAN and Area X. The custom-made holder that carried
145 the Neuropixels probe was fixed to the skull with dental cement and the craniotomy was
146 sealed with a two-part silicone gel (Dow Dowsil™) before it was covered with a custom-
147 made casing. In order to fix the Neuropixels headstage to the bird's head in a natural
148 position, the bird's head was rotated to a 35-degree angle in the stereotaxic during the
149 fixation. Finally, the ground wire was connected and open holes along the implant were
150 sealed with fast drying two-component silicone gel (Kwik-Sil).
151 The weight of the implant (~1.9 g) was immediately offset by a weight-relieving system. The
152 headstage was connected to an external counterweight using a nylon thread that was routed
153 through simple guide points positioned above and to the side of the setup, forming an
154 inverted U-shape. This allowed the counterweight to remain outside the recording area while
155 still providing vertical support and offsetting the implant's weight. The counterweight was
156 manually adjusted to ensure that the animals could move comfortably and were not
157 burdened by the implant.

158 **Histology**

159 Post-hoc control of the electrode location in the brain was performed through histological
160 examination of brain tissue. At the end of the experiment, birds were given a lethal injection
161 (i.p) of Exagon (pentobarbital sodium, 400 mg/mL), and in some cases perfused
162 intracardially (0.01 M Phosphate-Buffered Saline (PBS) followed by 4% paraformaldehyde
163 (PFA)). The brain was removed and post-fixed in 4% PFA for at least 24 hr. For 2 birds
164 recorded in Bordeaux, the brains were subsequently cryoprotected in 30% sucrose and cut
165 using a freezing microtome; for 3 birds recorded in Paris, brains were cut fresh at room
166 temperature using a vibratome. In all cases, the right hemisphere was cut in the sagittal
167 plane at a thickness of 50-80-microns. Images of the individual brain slices were taken using
168 bright-field and epiflurescence microscopy and analyzed using ImageJ software (Rasband
169 WS, NIH, Bethesda, Maryland, USA). The electrode track as indicated by

170 colored/fluorescent dye, was clearly visible on consecutive brain slices (see Fig. 1C; tissue
171 from ZF2 and prepared on a vibratome).
172 2 birds died during the Covid-19 laboratory lockdown, and we were not able to retrieve the
173 brains in time to perform histology (Table 1). For these animals, the channel assignment was
174 performed on the basis of the electrophysiology, as described in detail below.
175

176 **Electrode channel mapping**

177 We defined the boundaries of LMAN and Area X based on darkness of the tissue in regular
178 light or the fluorescent background, as these two brain areas showed a clear contrast with
179 surrounding tissue due to higher myelination, cell density, and size (Nixdorf-Bergweiler et al.,
180 2007). The reconstruction of electrode channels to be assigned to LMAN or X was
181 performed based on the location of the electrode tip on the histological pictures, the
182 coordinates of the channels on the electrode and the above-mentioned boundaries of LMAN
183 and X. The limits of LMAN were also confirmed based on spontaneous activity, including
184 more bursts of large spikes in LMAN as compared to surrounding tissue.

185 For the 2 birds with missing histology, we relied heavily on these electrophysiological
186 properties, including the spike amplitude, rate, and response mapping that was performed
187 during the surgical probe implantation. Generally, LMAN channels were associated with
188 larger spike amplitudes, whereas Area X channels had higher spike rates.

189 **Experimental design**

190 Animals were housed individually in sound-attenuated recording chambers and neural
191 recordings were performed in sessions (one to 24 hours of continuous neural recording).

192 **Electrophysiology**

193 Extracellular activity was recorded with the chronically implanted Neuropixels 1.0 probe
194 which splits the signal on chip and samples the spike signal (bandpass filtered at 0.3 and 10
195 kHz) at 30 kHz and the LFP signal (bandpass filtered at 0.5 and 500 Hz) at 2500 Hz. Audio

196 signals were simultaneously recorded using a wall-attached microphone, pre-amplified and
197 digitized at 10, 20 or 32 kHz depending on the bird.

198 **Sleep Recordings**

199 Sleep-related activity was recorded either continuously throughout the night (n=3 birds;
200 Table 1) or at the beginning or end of the night (n =4). In the case of continuous recordings,
201 a one-hour segment was selected by visually inspecting the microphone data for a
202 consolidated quiet period indicative of sleep. In 5 out of 7 birds, sleep-related activity was
203 recorded with the lights off during the normal dark period; however, in 2 birds (see Table 1),
204 the dark period was initiated earlier than normal, and recording sessions started in the late
205 afternoon (with lights off).

206 **Awake Recordings**

207 For 4 out of the 7 birds (ZF-1, ZF-2, ZF-3 and ZF-5), we also examined brain activity that
208 occurred during normal daytime hours in the light. The behavior of the birds during this time
209 was characterized by singing, active movement, and periods of rest. Because it was possible
210 that birds were napping during periods of daytime rest, we classified the awake data into two
211 behavioral states on the basis of sounds detected from the microphone. “Light on active"
212 periods corresponded to microphone data which contained singing or sounds related to
213 movements. (These periods were distinct from movement-related voltage artifacts which
214 were detected as described below in section “Sound detection and movement artifact
215 identification”). “Light on rest" periods corresponded to microphone data where no sounds
216 were detected, and during which the bird could have been in a state of quiet daytime rest
217 (see section “Sound detection and movement artifact identification” and Table 2 for more
218 information).

Statistical analysis

Data preprocessing and spike clustering

For neural spiking analysis, spike sorting was performed in four of the seven birds on all active channels using Kilosort 1.0 and Kilosort 2.5 (Pachitariu et al., 2016) and manually curated using phy (https://github.com/kwikteam/phy) in four birds (ZF-1, ZF-2, ZF-3 and ZF-5) or automatically curated using SpikeInterface (script available in our data repository) in one bird (ZF-4).

Sound detection and movement artifact identification

We identified periods of putative awakening during the lights-off period by analyzing the microphone recordings. We calculated the root mean square (RMS) of the microphone signal and manually defined a threshold that was just above the noise level (Fig. 3A, Fig. S1). Each threshold crossing identified a putative movement-related sound, and 1-s bins during which sound was detected were excluded from further analysis.

It is possible that during the lights-off recordings that the bird could awaken briefly but not move, which would not be identified as a putative awakening by our sound detection approach. Therefore, it might be that some of our analysis is not purely sleep and may include periods of quiet rest in the dark.

For the analysis of awake neural activity, we similarly leveraged the microphone recording to distinguish between silent periods and periods of activity. Periods where sounds were detected were identified as “Lights on active” periods, and silent periods were identified as “Lights on rest.”

The awake data often exhibited movement-related artifacts in the LFP which we did not observe in the putative sleep recordings. These daytime movement artifacts were characterized by synchronous fluctuations across all channels. To address this, we applied a modified version of the Artifact Subspace Reconstruction (ASR, (Chang et al., 2020; Kothe & Makeig, 2013) algorithm to identify and exclude artifact-contaminated periods. Briefly, we

246 performed an eigenvalue decomposition of the data covariance matrix. Components
247 associated with large eigenvalues indicative of high-variance noise, were flagged as
248 potential artifacts. These eigenvalues were identified using a threshold defined as a multiple
249 *q* of the median eigenvalue. To detect specific times of contamination, we reconstructed the
250 LFPs using only the artifact-related components and computed the summed signal across all
251 channels. Time bins where this signal exceeded a threshold—defined as the mean plus *k*
252 times the standard deviation—were marked as contaminated and excluded from further
253 analysis. Both *k* (ranging between 3 and 12) and *q* (ranging between 10 and 30) were
254 manually tuned for each bird to conservatively exclude movement artifacts without
255 discarding valid neural activity.

256 **Sleep staging**

257 The sleep staging was performed using an unsupervised k-means clustering algorithm
258 previously developed in songbirds to classify sleep data on the basis of multiple EEG
259 features (Canavan & Margoliash, 2020; Low et al., 2008). This algorithm classifies sleep into
260 one of 3 states: SWS, REM sleep, and intermediate sleep (IS) which has been compared to
261 the mammalian NREM sleep stage N2 and often contains a mixture of low-amplitude delta
262 and higher-frequency elements such as theta (Canavan & Margoliash, 2020). We computed
263 the sleep stages from an LMAN LFP channel (identified as a centrally located LMAN channel
264 along the dorsoventral axis of recording) using 3 s bins (1 s overlap). Spectral parameters
265 were computed from the multi-taper spectral analysis (Prerau et al., 2017) of the filtered (0.5
266 - 60 Hz) and down sampled (250 Hz) LFP. A small number of bins were not classified as
267 REM, SWS or IS using the two-step clustering algorithm (Canavan & Margoliash, 2020) and
268 were labeled 'Not classified/Nc'. Nc classifications arise when a bin is classified as SWS in
269 the first clustering round and then as REM in the second clustering round.
270 Our use of a centrally located LMAN LFP channel to classify sleep stages (instead of a
271 superficially located EEG electrode) means that our sleep staging results may diverge
272 slightly from values reported elsewhere (Canavan & Margoliash, 2020; Low et al., 2008;

Yeganegi & Ondracek, 2023, 2025). However, LFP signals were filtered in the same way that EEG signals were filtered (i.e., between 0.5 and 60 Hz), which would eliminate high-frequency characteristics that might be present in an LFP recording but not in an EEG recording.

Another concern was that the LFP recording centered in LMAN might not reflect “global” sleeping activity. Indeed, recent work has shown that sleeping brain dynamics are not as global as previously thought, and different sleep states might occur in different brain regions, as was also reported for songbirds (Yeganegi & Ondracek, 2025). To investigate this in our own data (Fig. S2), we examined the differences in sleep classifications in a superficial LFP located in the hyperpallium (comparable to a superficially implanted EEG electrode) and compared it to a centrally located LMAN channel (Fig. S2A). We found that almost 90% of the sleep scoring matched between the LMAN channel and the superficial LFP channel (Fig. S2B), suggesting that the use of an LMAN channel to assess sleep state is a fair assessment of the ongoing sleep states that would have been recorded using a superficial EEG electrode. Of the 11% of mis-matched sleep states, the largest category involved a mismatch between SWS and IS, such that sleep states that were identified as SWS in LMAN were identified as IS in the hyperpallium (Fig. S2C).

LFP Coherence Analysis

Data inclusion

For the coherence analysis we only used bins identified as either REM or SWS. Time points at which movements were detected, as described in the previous section (Sound detection and movement artifact identification) were excluded for the coherence analysis.

LFP pre-processing

First, we extracted the LFP data from *.bin* files utilizing SpikeInterface (https://spikeinterface.readthedocs.io/en/latest/overview.html) with phase shift correction using *spikeinterface.preprocessing.phase_shift*. Next, we removed artifacts from the LFP

signal by establishing a threshold based on 80% of the maximum absolute trace value and interpolating the signal around the artifact time point with a margin of 20 samples before and after. Next, we z-scored the trace using *elephant.signal_processing.zscore.*

Coherence Analysis – Sleep recordings

Pairwise LFP coherence was computed from the z-scored LFP traces. We included every 4th LFP channel (corresponding to a dorso-ventral linear distance of approximately 40 microns between them) spanning Area X and LMAN to reduce the computation time while still retaining enough spatial resolution to obtain a clear estimate of the spatial variation. We performed pairwise LFP coherence per identified state. For sleep recordings, this involved computing coherence for the SWS and REM states respectively. Specifically, we computed the magnitude squared coherence $C_{1,2}$ of LFP signals L1 and L2 as follows:

$$C_{1,2} = {\left|P_{1,2}\right|^2}\Big/{P_{1,1}\,P_{2,2}}$$

where $P_{1,1}$ and $P_{2,2}$ are power spectral density estimates of L1 and L2 using Welch's method, and $\left|P_{1,2}\right|$ is the absolute value of the cross spectral density estimate. We used the *scipy.signal.coherence (https://docs.scipy.org/doc/).*

The accuracy of coherence magnitude estimates depends on 1) the length of the segments used for computation that is usually determined by the lowest frequency of interest (FOI) and 2) the total number of such segments obtained (equal to the total length of the signal being analyzed divided by the segment length). In our case, these parameters were constrained by our lowest FOI which was 1 Hz and the total duration of REM or SWS states in our recordings per bird. We selected a segment length of 3 sec for our analysis, since 3 sec segments were sufficient to give an accurate coherence estimate for our lowest FOI (1 Hz) and our total length of recordings corresponding to SWS or REM were large enough to obtain sufficient number of 3-sec segments.

After accounting for removal of movement artifacts and the analysis of only the REM and SWS segments, the total percentage of data analyzed in the coherence analysis per bird were: ZF1: 78.2%, ZF2: 78.4%, ZF3: 65.9%, ZF4: 76.2%, ZF5: 85.8%, ZF6: 77.4%, ZF7: 71.4%. Because the number of SWS segments were more numerous that the number of REM segments, for each channel comparison, we initially performed the coherence computation using a randomly selected number of SWS segments equal to the total number of REM segments. We then averaged across all SWS segments after ascertaining that the standard error of mean for the averaged coherence for all the SWS segments was low (< 0.05 for all channel comparisons for all birds) indicating low variation between randomly selected SWS segments.

In order to evaluate statistical significance in the coherency analysis between SWS and REM states, we first selected a minimum number of channels to compare that was the same for all birds for each brain area (LMAN = 7; equal to ~240 microns, Area X = 26; equal to ~1000 microns). This was necessary as the probe implantation was variable across animals and resulted in different number of total channel counts in the brain areas of different birds. Then we identified the most central channel in each brain area and included neighboring channels along the probe length. After pooling these channel comparisons across birds for SWS and REM states, we identified significant differences across brain states in the coherence analysis using a Wilcoxon Signed Rank test.

Coherence Analysis – Awake recordings

A similar procedure was followed for analysis of the awake daytime recordings (obtained from 4 out of the 7 birds). Here our goal was to determine whether behavioral state affected the coherence between brain areas. That is, we compared sleep-related activity to periods of Light on active and Light on rest states. Only 3 out of the 4 birds (ZF-1, ZF-2, and ZF-4) had sufficiently long periods of both Light On states to allow us to compare the pair-

wise coherence analysis (see Table S1 for more information). Coherence values were pooled across birds as described above. To compare the awake and putative coherence results for these 3 birds, we performed statistical testing using a Friedman Test followed by the Nemeyni posthoc tests to account for multiple comparisons between non-independent samples (same channels and 4 different behavioral states.

Analysis of spiking variability

To assess how spike activity varied over time within LMAN and Area X during putative sleep, we computed the coefficient of variation (CV) in consecutive, non-overlapping segments of 10 seconds. Within each segment, we counted the total number of spikes (ns, from all units either in LMAN or in Area X) in sub-windows of 20 milliseconds. The CV was then computed as the standard deviation of spike counts divided by the mean spike count across all sub-windows within that segment (CV $=\sigma_{ns}/\mu_{ns}$). Because we were interested in the relationship between the temporal variability of spike activity within a population and how it related to putative sleep, we computed the δ/γ ratios for the LFP signal of the central electrode in LMAN in the same 10-second segment. We then used Pearson's correlation coefficient (Pearson, 1895) and type-II linear regression (Ricker, 1973) to assess the relationship between δ/γ ratios and the CV of spike activation. The average firing rate of neurons in LMAN and Area X was calculated by determining the total spike count per second within the same windows where CV was computed. We performed this analysis for sleep recordings in five birds (ZF-1 to ZF-5), excluding segments that were contaminated by potential movement (see *Sound detection and movement artifact identification*).

Population synchronized burst detection and spectral analysis of associated LFP

For each neural unit (single or multiunit), bursts were identified when the Instantaneous Firing Rate (IFR) exceeded 100 Hz. The fraction of simultaneously bursting LMAN units was determined in a sliding 50 ms window with 10 ms step size. The resulting trace was

379 smoothed using a Gaussian kernel with 15 ms standard deviation, and candidate events of
380 synchronized bursts were classified as peaks exceeding the 99th percentile.
381 We performed this analysis for sleep-related recordings of five birds (ZF-1 to ZF-5). Events
382 that occurred during the 1-sec segments that were flagged as putative awakenings or Nc
383 sleep states were excluded. Similarly, in daytime recordings, events that overlapped with
384 LFP movement artifacts were also excluded (see *Sound detection and movement artifact*
385 *identification*).
386 To create control events, we used random time points in the recording. For assessing the
387 LFP around synchronized bursts and control time points, we selected the central LMAN LFP
388 and compared raw traces that were offset-corrected by median subtraction. Interested in a
389 high-resolution description of the non-stationary spectro-temporal content of the associated
390 LFP, we applied a complex wavelet transform using complex Morlet (Gabor) wavelets (*cwt,*
391 MATLAB, The MathWorks, Natick, MA). Scalograms were computed over a 1-sec window
392 centered on each event. Vice versa, to assess the oscillatory context of these events, we
393 calculated the power estimate in the δ- (1-4 Hz) and γ-band (30 – 90 Hz) in the 3-sec
394 window around the event, the same bin size used for sleep staging, using Thomson's
395 multitaper power spectral density method (*pmtm*, MATLAB, The MathWorks, Natick, MA).
396 For the high γ-band (90 – 145 Hz), we used a narrower window of 300 ms centered to the
397 event.
398

399 **Data and software availability**

400 All research data as well as scripts to replicate the results are available in the corresponding
401 repository: https://gin.g-node.org/E4-Leblois/npx_sleep_2024
402 Spectral analysis and visualizations in Figure 3 were computed with an adapted code of the
403 following repository https://github.com/cortex-lab/spikes.

Results

Distinct regimes of activity are present during avian sleep

We investigated neural activity in the pallium and basal ganglia of male zebra finches (n = 7) chronically implanted with Neuropixels 1.0 probes (Fig. 1B). In each animal, the probe was implanted such that both the pallial structure LMAN and the striatal structure Area X within the avian BG (Person et al., 2008) were targeted (Fig. 1C).

We observed that during putative sleep, slow wave delta activity (1-4 Hz) in the LFP was widespread throughout the pallium and BG, spanning more than 4 mm (Fig. 1D, black arrowheads). Neural spiking was synchronized with the slow wave dynamics and was observable as sparsely bursting patterns of activity in both pallial and BG neurons (Fig. 1D-Spiking Activity). These slow wave dynamics and periods of synchronized bursting were entirely absent from awake data (Fig. 1 E).

We used two complementary approaches to further analyze putative sleep states: 1) we analyzed sleep as a continuous variable using the LFP δ/γ power ratio, and 2) we categorized sleep into discrete stages using an automated avian sleep clustering algorithm (Canavan & Margoliash, 2020; Low et al., 2008). Whereas the former approach acknowledges the continuous nature of sleeping brain dynamics, the latter approach allowed us to numerically characterize certain aspects of avian sleep and compare our results with other avian sleep studies.

To analyze the continuous nature of sleeping brain dynamics, we calculated the δ/γ ratio as the ratio of delta activity (δ, 1-4 Hz) to gamma activity (γ, 30-90 Hz). This method is analogous to metrics that have been used with rodents (Csicsvari et al., 1998; O'Keefe,

429 1976), but accounts for the dominant frequency bands present during avian sleep (Low et
430 al., 2008; Yeganegi et al., 2019; Yeganegi & Ondracek, 2023).
431
432 We calculated the δ/γ ratio for a large range of pallial and BG sites (Fig. 2A). Whereas δ/γ
433 ratios calculated for LFPs within the BG were mostly flat (Fig. 2A, blue lines), δ/γ ratios
434 calculated for pallial LFPs were large and dynamic (Fig. 2A, pink lines, also black line).
435 Within the pallium, we observed that LPF traces with low δ/γ values had REM sleep-like
436 characteristics (i.e., low amplitude LFP signals), while LFP traces with high δ/γ had SWS-like
437 characteristics (i.e., large amplitude LFP signals; Fig. 2B). Median δ/γ values, calculated
438 using a centrally located pallial LMAN LFP for each bird individually, showed some variability
439 across birds (Fig. 2C) but were within the range of values previously reported using similar
440 metrics (Yeganegi & Ondracek, 2023, 2025). We used the centrally located LMAN channel
441 quantified in Fig. 2C for all subsequent analysis using the δ/γ ratio.
442 In addition to the δ/γ ratio, we used a clustering-based sleep scoring method (Canavan &
443 Margoliash, 2020; Low et al., 2008) to classify sleep stages (see Methods for more details).
444 For this analysis, we used the same centrally located LMAN channel that we used in the δ/γ
445 analysis. We observed LFP segments that were classified as SWS were indeed
446 characterized by high δ/γ values, and LFP segments that were classified as REM sleep were
447 characterized by low δ/γ values (Fig. 2D, E) with IS states falling in between the two
448 distributions (Fig. 2F). 3-D plots showed that sleep states were well-segregated on the basis
449 of the spectral features used in the clustering-based approach (Fig. 2G, H). See Fig. S3 for
450 sleep classification distributions for all birds.

451 Different spectral features characterize sleep and awake states

452 Were the activity patterns that we observed during sleep different than those observed
453 during wakefulness? In the next analysis, we examined the spectral features of the LFP
454 signals recorded in LMAN and the surrounding pallium as well as Area X and the
455 surrounding BG during awake and putative sleep phases (Fig. 3A, B). In contrast to the

456 sleep-related activity which was recorded in the dark, the awake recordings took place in the
457 light during the normal day-time hours and captured awake behavior (e.g., singing, moving,
458 resting; Fig. S1).
459 We observed in LMAN (Fig. 3C, dark gray shading) and the surrounding pallial channels
460 (Fig. 3C, light gray shading) that the power was higher for a broad range of low frequencies
461 during sleep compared to awake states (Fig. 3C, 1-4 Hz, 4-12 Hz, 12-30 Hz, black
462 arrowheads, thin line compared to thick line). In contrast, for LFPs recorded within Area X
463 (Fig. 3C, dark green shading) and the surrounding BG (Fig. 3C, light green shading) only the
464 power in the theta range (Fig. 3C, 4-12 Hz) was occasionally higher during putative sleep
465 compared to awake states (Fig. 3C, black arrowhead, thin line compared to thick line; see
466 also Fig. S4 for data from other birds).
467 The power in the high-frequency gamma range (Fig. 3C, 90-145 Hz) was higher for LMAN
468 LFPs during awake states compared to sleep states in all birds (Fig. 3C, black arrowhead,
469 see also Fig. S4).
470
471 Across depths, we saw that putative sleep states were associated with higher power in low
472 frequency bands compared to awake states (Fig. 3D), which is in line with results from brain
473 areas including RA (Hahnloser et al., 2006) and Area X (Yanagihara & Hessler, 2012).
474 Importantly, the LFP associated with the LMAN depth (Fig. 3D, black line; 2.6 mm) was
475 strongly modulated by sleep. We saw that LFPs at the deepest part of the probe followed the
476 common 1/f power spectrum but generally carried less power (Fig. 3D, light green line: 0.1
477 mm from probe tip).

478 Within-area coherence is high during SWS in LMAN and Area X

479 Given the clear spectral differences that we observed between LMAN and Area X during
480 sleep and awake states, we focused our next analysis on investigating the functional
481 connectivity between these brain areas. We characterized the LFP coherence 1) within

482 LMAN, 2) within Area X, and 3) across LMAN and Area X for 3-s SWS and REM sleep LFP
483 segments and for different canonical frequency ranges that have been shown to play an
484 important role in behavior (Buzsáki & Draguhn, 2004) for all birds (Fig. 4A, B).

485 We observed the average pairwise LFP coherence across birds to be significantly modulated
486 by sleep states (Fig. 4B, Fig. 4C). Whereas coherence in the low frequency ranges was
487 spatially widespread during SWS (Fig. S5), gamma band coherence was limited to spatially
488 neighboring channels with the coherence values dropping to 50% of its peak value within
489 150 microns. This is consistent with the idea that gamma oscillations reflect local network
490 dynamics (Buzsáki & Wang, 2012; Cardin, 2016; Cardin et al., 2009).

491 Since the pairwise LFP coherence varied as a function of the distance between the electrode
492 sites and the total number of electrodes within brain regions varied slightly across birds due
493 to variations in implant angle or exact implant co-ordinates, we compared the same number
494 of LMAN and Area X electrodes sites across birds to compare the median coherences
495 between sleep states. The sites were selected such that they spanned the same distance
496 from the identified centers of these brain areas for all 7 birds (see Methods for more details).

497 We found that SWS and REM sleep coherence values were significantly different for all
498 frequency bands analyzed and across all brain areas (Fig. 4D; Table 2). During SWS within
499 LMAN, we observed very high delta band coherence, ranging from 0.86 - 0.99 (min - max,
500 median = 0.96; Table 2). During REM sleep within LMAN, the delta band coherence was still
501 high (median = 0.87), but the range of values was larger (0.63 - 0.99; min - max), indicating
502 a decrease in coherence between some LMAN pairs during REM sleep.

503 Within Area X, median coherence values were lower for all frequency ranges and sleep
504 states compared to within LMAN coherence values (Fig. 4B, C; Table 2). Median coherence
505 values within Area X were lower during REM sleep compared to SWS for all frequency
506 ranges (Fig. 4C, Fig. 4B green dots). This finding is consistent with primate literature

507 demonstrating significantly lower coherence within basal ganglia compared to cortical areas
508 during SWS (Mizrahi-Kliger et al., 2018).

509 LMAN sends direct projections to Area X, which in turn sends feedback projections to LMAN
510 through thalamic area DLM (Fig. 1A; (Farries et al., 2005). If the closed-loop structure of the
511 circuit plays an important role in modulating sleep dynamics, we may expect strong cross-
512 area coherence.

513 While median coherence values were low across frequency bands for LMAN-Area X LFP
514 pairs compared to within-LMAN or within-Area X LFP pairs (Table 2), a few individual LMAN-
515 Area X LFP pairs showed high coherence values > 0.5, especially for the low frequencies (1-
516 12 Hz; Fig. 4B, blue dots). This finding suggests that the input from LMAN to Area X may be
517 spatially restricted, as only a few pairs shared similar oscillatory drive during sleep.

518 We did not find a strong effect of sleep state on the across-area LMAN-Area X coherence.
519 Although significant differences were found across all frequency bands (Fig. 4C, right), the
520 median differences between SWS and REM sleep were quite small (Table 2).

521

522 LMAN-Area X dynamics are modulated by behavioral state

523 We were curious as to how the LFP coherence changed as an effect of behavioral state, and
524 so we compared the sleep-related LFP coherence with coherence analyzed for daytime
525 “Light on awake” and “Light on rest” periods for a small group of birds (n=3 birds; Fig. 4D).
526 The sleep-related coherence analysis for this smaller group of birds was consistent with the
527 results of the larger group of seven birds (see Table S2): coherence values were highest
528 within LMAN compared to within Area X and across LMAN and Area X pairs for all frequency
529 bands, and coherence values were higher during SWS compared to REM sleep across
530 frequency bands, with the exception of high gamma within LMAN. In this case, REM

531 coherence was higher compared to SWS coherence within LMAN; however, this difference
532 was not significant for the smaller group of three birds (Fig. 4D, LMAN-LMAN comparison;
533 High gamma, n.s.).

534 When we compared sleep-related coherence to daytime coherence (i.e., Light on active and
535 Light on rest), we saw that the delta and theta band coherence values were significantly
536 lower for daytime periods, suggesting that periods of putative sleep in the dark (i.e., SWS
537 and REM states) were distinct from periods of active and quiet rest recorded during the
538 daytime.

539 Interestingly, when we analyzed the coherence trends within the daytime periods, we
540 observed that periods of daytime active behavior were associated with higher delta band
541 coherence values compared to periods of daytime rest. This was true for within LMAN, within
542 Area X, and across LMAN-Area X LFP pairs, suggesting that daytime rest periods may not
543 have necessarily captured periods of daytime napping.

544 Phases of high δ/γ activity during sleep are associated with 545 increased spiking variability for neurons in LMAN but not Area X

546 Using our Neuropixels recordings, we leveraged the high-pass filtered electrode signals to
547 investigate the spiking activity in LMAN and Area X during sleep in n = 5 birds (Table 1).
548 Spikes were identified and assigned using state-of-the-art automatic detection and sorting
549 algorithms, either in a fully automated way or followed by meticulous manual curation to
550 ensure accuracy and reliability (see Methods). The results of any spiking analysis did not
551 differ qualitatively across these two preprocessing approaches.
552

553 During sleep, we observed increased but sparse population-wide spiking activity which was
554 locked to negative LFP deflections and interleaved with periods of neural silence, followed
555 by sudden switches to periods of random spiking and lower LFP amplitudes (see Fig. 1D).
556 To quantify the different patterns of spiking activity that we observed during sleep, we

557 calculated the coefficient of variation (CV, standard deviation divided by the mean) for
558 identified LMAN and Area X neuron populations in 10 ms bins.
559
560 The CV can be thought of as a measure of collective variability in coincident spike trains: CV
561 values for the population rate will approach zero when all neurons are statistically
562 independent (Kobak et al., 2019). This is because random irregularities stemming from
563 individual neurons will average out as the population size increases, ultimately leading to a
564 stable population rate. However, when neurons are synchronized and activity oscillates, the
565 variability from one moment to another in the population rate is high.
566
567 We found that median CVs ranged from 0.27 in Area X to 2.14 in LMAN (Fig. 5A; see Table
568 3 for individual values), and CV values were significantly higher for LMAN neurons
569 compared to Area X neurons in all birds (median [min, max] LMAN CV over all birds = 1.44
570 [0.73, 2.14]); median [min, max] Area X CV for all birds was = 0.61 [0.27, 1.04]).
571
572 We observed that the CV values fluctuated closely with δ/γ values, such that high CV values
573 were associated with high δ/γ values (Fig. 5B). This trend was especially obvious for LMAN
574 neurons (Figure 5C, D). Indeed, regression fits between CV values for LMAN neurons and
575 δ/γ values returned higher slopes (Fig. 5C, D) and both variables were highly correlated for
576 all birds (Table 4). This was not the case for Area X neurons: estimated regression slopes
577 were lower, and only 2/5 birds showed significant positive correlations between CV values
578 and δ/γ values (ZF-1 and ZF3), whereas 1 bird showed a significant negative correlation
579 (ZF-4, Table 4; Fig. 5C, filled symbols).
580
581 High CV values for LMAN neurons compared to lower CV values for Area X neurons (Fig.
582 5A) suggest that the spike trains for LMAN neurons were more irregular than for Area X
583 neurons. Indeed, when we examined spike rasters corresponding to high CV values for
584 LMAN populations (Fig. 5D, E), spiking patterns were conspicuously irregular - albeit largely

synchronized as bursts of spikes across the population of LMAN neurons. In contrast, CV values were significantly lower for Area X neurons (Fig. 5A), capturing their regular spiking patterns and high firing rates (Fig. 5D, F).

It is important to note that the δ/γ trace used in this analysis was calculated from a centrally located LMAN LFP (see Methods for details). Therefore, strong correlations between CV values and δ/γ values in LMAN may reflect the tight correspondence between spiking activity and LFP oscillations in LMAN. The correspondence between spiking activity in Area X and the LMAN LFP was much more heterogeneous, suggesting that oscillatory activity in LMAN did not directly influence Area X spiking activity during sleep as it did in LMAN.

Synchronized population bursting in LMAN during sleep is associated with a negative deflection in the LFP

Our findings suggested that within LMAN, populations of neurons are co-activated at specific time points during putative sleep. In order to explore the synchronized bursting of LMAN neurons during putative sleep - and how they are related to the LFP (Fig. 6A) - we identified and thresholded bursting events in the population of LMAN neurons (Fig. 6B). Then, we used these synchronized bursts to identify activity patterns in the LFP, which we called “burst-aligned LFP” (Fig. 6C). Individual burst-aligned LFP segments generally had higher power in frequency ranges < 10 Hz (example in Fig. 6D), and the average burst-aligned LFP showed a prominent low-frequency power burst centered on zero-time lag (Fig. 6E). Indeed, when we compared the bursting-aligned LFP segments (Fig. 6C, lower blue line) to randomly selected LFP segments (Fig. 6C, lower black line), the bursting-aligned LFP segments showed a notable increase in power for frequencies lower than 10 Hz. This phenomenon was present across birds: every bird examined had a notable negative deflection that corresponded to the population synchronized bursting (Fig. 6F).

611 Having established that synchronized bursting in LMAN during putative sleep is consistently
612 associated with prominent low-frequency deflections in the LFP, we next asked whether
613 similar events occur during wakefulness. Specifically, in the four birds for which we recorded
614 neural activity during daytime periods, we examined whether synchronized LMAN bursting
615 events also occur during active and resting periods, and if so, whether the associated burst-
616 aligned LFP exhibits features similar to those observed during putative sleep.
617
618 During light on rest periods, burst-aligned LFPs in ZF-2 and ZF-3 resembled those seen
619 during putative sleep, exhibiting a negative deflection in the LFP at the time of the
620 synchronized bursting and elevated low-frequency power in the scalogram, although with
621 reduced overall magnitude (Fig. 6G; Fig. S6). In contrast, ZF-1 exhibited no detected events
622 during rest, and ZF-5 showed only 11 events, none of which were associated with a clear
623 LFP deflection.
624
625 In active light-on periods, we observed numerous synchronized bursting events across all
626 birds except ZF-3, which was generally inactive during this recording (Fig. S1). The detected
627 events coincided with behaviors such as singing, calling, or general movement, consistent
628 with the increased bursting activity characteristic during vocal production (Hessler & Doupe,
629 1999). However, the associated LFPs remained flat across all birds, showing no consistent
630 deflection time-locked to the bursts (Fig. 6G, long dashed line; Fig. S6). This absence of
631 coordinated low-frequency structure in the LFP distinguishes these active-state bursting
632 events from those observed during putative sleep, where synchronized bursts are reliably
633 coupled with prominent negative LFP deflections (Fig. 6F).
634
635 Consistent with these observations, Fig. 6H summarizes the average LFP amplitude at the
636 time of synchronized bursts across states, showing the strongest negative deflections during
637 putative sleep, weaker deflections during light-on rest, and values near zero during active

638 wakefulness. This graded pattern supports a state-dependent modulation of LFP responses
639 to synchronized bursting in LMAN.

640 Synchronized population bursts in LMAN occur predominantly
641 during NREM sleep

642

643 We were curious as to whether these synchronized bursting events in LMAN occurred during
644 a specific sleep regime, i.e. either during NREM sleep (i.e., SWS and IS sleep) or during
645 REM sleep (Fig. 7A). With the exception of 1 bird (Fig 7A, ZF-4: upward triangle), the
646 synchronized bursting events occurred predominantly during NREM sleep.

647

648 We also examined the δ/γ values surrounding the synchronized bursting events, with the
649 expectation that these events might occur during LFP segments with higher δ/γ values (i.e.,
650 during SWS). Interestingly, we found that the bursting events were not consistently
651 associated with lower δ/γ values compared to control events across birds (Fig. 7B; see
652 Methods for details). Because the δ/γ is a ratio, low δ/γ values can result from a decrease in
653 δ power or an increase in γ power. We examined the δ and γ power separately for bursting
654 events compared to control events. We found that while the power in the δ range was indeed
655 elevated during bursting events compared to control events for all but one bird, ZF-4, (Fig.
656 7C), a larger increase in γ power during the bursting event (Fig. 7D) compared to control
657 segments led to the overall inconsistent δ/γ values we observed during bursting events
658 compared to controls (Fig. 7B).

659

660 When visualized as the difference between the burst and control segments (Fig. 7E), this
661 burst-associated increase in power extended from delta up through high gamma and was
662 present for all birds analyzed (Fig. 7F).

Discussion

In order to explore the ongoing spontaneous activity patterns of the AFP during putative sleep and awake behavior in songbirds, we investigated the sleep-related activity patterns of neurons in LMAN and Area X (Fig. 1A, C) using chronically implanted Neuropixels probes (Fig. 1B).

Coherence between field potentials has been used in a multitude of studies as a mesoscopic measure of functional connectivity between brain areas (Schneider et al., 2021) and is believed to reflect the neuronal connectivity (Buzsáki & Schomburg, 2015) and oscillatory synchronization (Bastos et al., 2015) in these brain areas. Contrary to our expectations, we did not observe strong across-area coherence between LMAN and Area X on average, although individual LMAN-Area X pairs did show strong coherence > 0.5. In contrast, studies of motor skill learning in rodents found an increase in cross-area coherence between motor cortex and striatum during sleep (Koralek et al., 2013; Lemke et al., 2021). The fact that we did not observe strong cross-area coherence may stem from the fact that the birds in this study were not actively engaged in a learning paradigm.

A previous study demonstrated the presence of phasic LFP gamma oscillations in Area X during sleep, with singing-modulated Area X units phase-locked to gamma oscillations (Yanagihara & Hessler, 2012). Our pairwise LFP coherence results, albeit a mesoscale measure of synchronization across brain areas, could be a reflection of this phase-locking and the concerted activity of anatomically connected LMAN units and Area X units during awake periods. Verification of this hypothesis would require further data collection in awake and singing birds to investigate the specific neural activity of different neuronal subtypes and their relation to the ongoing LFP gamma oscillations.

During putative sleep, we observed that populations of LMAN neurons spontaneously reactivated in bursting events. These events occurred predominantly during NREM sleep and were associated with a transient increase in gamma band power. Across animals, the

population bursting events were preceded by a large negative deflection of the LFP, pointing to the possibility that they were triggered by the ongoing large-scale global oscillatory activity in LMAN.

The combination of large negative LFP deflection and population bursting activity in LMAN is highly reminiscent of SWR activity observed during SWS and quiet rest in rodent hippocampus (Buzsáki, 1986, 2015; O'Keefe, 1976).

Importantly, the sharp wave and ripple LFP patterns that characterize mammalian SWRs are thought to arise from the specific anatomy of the hippocampus. The sharp wave reflects massive excitation of CA1 neurons by the pyramidal cells in CA3. This excitation synchronizes the interneuron network and generates a ripple in the pyramidal layer (Buzsáki et al., 1983; Girardeau & Zugaro, 2011; Liu et al., 2022). In rodents, the ripple oscillation is characterized by a frequency in the range of 110-200 Hz, overlapping with typical gamma band activity (Buzsáki, 2015; Liu et al., 2022).

Our observation of SWR-like activity in LMAN suggests that sharp waves coinciding with gamma oscillations may not be unique to mammalian hippocampus. Indeed, similar LFP patterns have been recorded during sleep in the reptilian pallial area known as the dorsal ventricular ridge (Albeck et al., 2022; Libourel et al., 2018; Shein-Idelson et al., 2016), suggesting that multiple neural architectures may give rise to these activity patterns. However, the function of this non-hippocampal SWR-like activity remains unclear.

Hippocampal SWR activity has been typically considered as a biomarker that accompanies spatial navigation learning and episodic memory (Buzsáki, 2015); these learning paradigms are fundamentally different from the auditory and motor learning that characterizes vocal learning in songbirds. Furthermore, the birds used in our study sang mature crystallized songs characterized by stable motif structure, suggesting that the developmental learning

period had already ended. Nevertheless, LMAN has been shown to have an important role in the ongoing maintenance of adult song via N-methyl-D-aspartate (NMDA) receptor-dependent transmission from LMAN to the pallial premotor nucleus RA (Brainard & Doupe, 2000; Solis et al., 2000; Warren et al., 2011). Bursting in LMAN influences RA and thereby affects the spectral variability of song (Kao et al., 2005; Moorman et al., 2021; Tian et al., 2023; Woolley & Kao, 2015). From these observations a potential role of avian SWR activity emerges in the consolidation of experience in a broader sense (Tachibana et al., 2022).

However, it remains to be determined whether the LMAN synchronized bursts that we observed during sleep represent true replay events related to, for example, daytime singing. “Replay”-like reactivations have also been reported during sleep in RA (Dave & Margoliash, 2000; Elmaleh et al., 2021, 2023). Given the widespread LFP dynamics that we observed across LMAN, it would be important to investigate how bursting in LMAN and RA are temporally related, and specifically whether the widespread LFP oscillations in LMAN influence RA bursting during sleep.

References

Albeck, N., Udi, D. I., Eyal, R., Shvartsman, A., & Shein-Idelson, M. (2022). Temperature-robust rapid eye movement and slow wave sleep in the lizard Laudakia vulgaris. *Communications Biology*, *5*(1), Article 1. https://doi.org/10.1038/s42003-022-04261-4

Ali, F., Otchy, T. M., Pehlevan, C., Fantana, A. L., Burak, Y., & Ölveczky, B. P. (2013). The Basal Ganglia Is Necessary for Learning Spectral, but Not Temporal, Features of Birdsong. *Neuron*, *80*(2), 494–506. https://doi.org/10.1016/j.neuron.2013.07.049

Andalman, A. S., & Fee, M. S. (2009). A basal ganglia-forebrain circuit in the songbird biases motor output to avoid vocal errors. *Proceedings of the National Academy of Sciences of the United States of America*, *106*(30), 12518–12523. https://doi.org/10.1073/pnas.0903214106

Bastos, A. M., Vezoli, J., & Fries, P. (2015). Communication through coherence with inter-areal delays. *Current Opinion in Neurobiology*, *31*, 173–180. https://doi.org/10.1016/j.conb.2014.11.001

Bottjer, S. W., Miesner, E. A., & Arnold, A. P. (1984). Forebrain lesions disrupt development but not maintenance of song in passerine birds. *Science (New York, N.Y.)*, *224*(4651), 901–903. https://doi.org/10.1126/science.6719123

Brainard, M. S., & Doupe, A. J. (2000). Interruption of a basal ganglia-forebrain circuit prevents plasticity of learned vocalizations. *Nature*, *404*(6779), 762–766. https://doi.org/10.1038/35008083

Buzsáki, G. (1986). Hippocampal sharp waves: Their origin and significance. *Brain Research*, *398*(2), 242–252. https://doi.org/10.1016/0006-8993(86)91483-6

Buzsáki, G. (2015). Hippocampal sharp wave-ripple: A cognitive biomarker for episodic memory and planning. *Hippocampus*, *25*(10), 1073–1188. https://doi.org/10.1002/hipo.22488

Buzsáki, G., & Draguhn, A. (2004). Neuronal Oscillations in Cortical Networks. *Science*, *304*(5679), 1926–1929. https://doi.org/10.1126/science.1099745

Buzsáki, G., Leung, L. W. S., & Vanderwolf, C. H. (1983). Cellular bases of hippocampal EEG in the behaving rat. *Brain Research*, *287*(2), 139–171.

Buzsáki, G., & Schomburg, E. W. (2015). What does gamma coherence tell us about inter-regional neural communication? *Nature Neuroscience*, *18*(4), 484–489. https://doi.org/10.1038/nn.3952

Buzsáki, G., & Wang, X.-J. (2012). Mechanisms of Gamma Oscillations. *Annual Review of Neuroscience*, *35*, 203–225. https://doi.org/10.1146/annurev-neuro-062111-150444

Canavan, S. V., & Margoliash, D. (2020). Budgerigars have complex sleep structure similar to that of mammals. *PLOS Biology*, *18*(11), e3000929. https://doi.org/10.1371/journal.pbio.3000929

Cardin, J. A. (2016). Snapshots of the Brain in Action: Local Circuit Operations through the Lens of γ Oscillations. *Journal of Neuroscience*, *36*(41), 10496–10504. https://doi.org/10.1523/JNEUROSCI.1021-16.2016

Cardin, J. A., Carlén, M., Meletis, K., Knoblich, U., Zhang, F., Deisseroth, K., Tsai, L.-H., & Moore, C. I. (2009). Driving fast-spiking cells induces gamma rhythm and controls sensory responses. *Nature*, *459*(7247), 663–667. https://doi.org/10.1038/nature08002

Chang, C.-Y., Hsu, S.-H., Pion-Tonachini, L., & Jung, T.-P. (2020). Evaluation of Artifact Subspace Reconstruction for Automatic Artifact Components Removal in Multi-Channel EEG Recordings. *IEEE Transactions on Biomedical Engineering*, *67*(4), 1114–1121. https://doi.org/10.1109/TBME.2019.2930186

Csicsvari, J., Hirase, H., Czurko, A., & Buzsáki, G. (1998). Reliability and state dependence of pyramidal cell-interneuron synapses in the hippocampus: An ensemble approach in the behaving rat. *Neuron*, *21*(1), 179–189. https://doi.org/10.1016/s0896-6273(00)80525-5

Dave, A. S., & Margoliash, D. (2000). Song replay during sleep and computational rules for sensorimotor vocal learning. *Science (New York, N.Y.)*, *290*(5492), 812–816. https://doi.org/10.1126/science.290.5492.812

Debas, K., Carrier, J., Barakat, M., Marrelec, G., Bellec, P., Hadj Tahar, A., Karni, A., Ungerleider, L. G., Benali, H., & Doyon, J. (2014). Off-line consolidation of motor sequence learning results in greater integration within a cortico-striatal functional network. *NeuroImage*, *99*, 50–58. https://doi.org/10.1016/j.neuroimage.2014.05.022

Duffy, A., Latimer, K. W., Goldberg, J. H., Fairhall, A. L., & Gadagkar, V. (2022). Dopamine neurons evaluate natural fluctuations in performance quality. *Cell Reports*, *38*(13), 110574. https://doi.org/10.1016/j.celrep.2022.110574

Elmaleh, M., Kranz, D., Asensio, A. C., Moll, F. W., & Long, M. A. (2021). Sleep replay reveals premotor circuit structure for a skilled behavior. *Neuron*, *109*(23), 3851-3861.e4. https://doi.org/10.1016/j.neuron.2021.09.021

Elmaleh, M., Yang, Z., Ackert-Smith, L. A., & Long, M. A. (2023). Uncoordinated sleep replay across hemispheres in the zebra finch. *Current Biology*, *33*(21), 4704-4712.e3. https://doi.org/10.1016/j.cub.2023.09.005

Farries, M. A., Ding, L., & Perkel, D. J. (2005). Evidence for “direct” and “indirect” pathways through the song system basal ganglia. *The Journal of Comparative Neurology*, *484*(1), 93–104. https://doi.org/10.1002/cne.20464

Farries, M. A., & Perkel, D. J. (2002). A Telencephalic Nucleus Essential for Song Learning Contains Neurons with Physiological Characteristics of Both Striatum and Globus Pallidus. *Journal of Neuroscience*, *22*(9), 3776–3787. https://doi.org/10.1523/jneurosci.22-09-03776.2002

Gadagkar, V., Puzerey, P. A., Chen, R., Baird-Daniel, E., Farhang, A. R., & Goldberg, J. H. (2016). Dopamine neurons encode performance error in singing birds. *Science*, *354*(6317), 1278–1282. https://doi.org/10.1126/science.aah6837

Girardeau, G., & Zugaro, M. (2011). Hippocampal ripples and memory consolidation. *Current Opinion in Neurobiology*, *21*(3), 452–459. https://doi.org/10.1016/j.conb.2011.02.005

Hahnloser, R. H. R., Kozhevnikov, A. A., & Fee, M. S. (2006). Sleep-related neural activity in a premotor and a basal-ganglia pathway of the songbird. *Journal of Neurophysiology*, *96*(2), 794–812. https://doi.org/10.1152/jn.01064.2005

Hessler, N. A., & Doupe, A. J. (1999). Social context modulates singing-related neural activity in the songbird forebrain. *Nature Neuroscience*, *2*(3), 209–211. https://doi.org/10.1038/6306

Jun, J. J., Steinmetz, N. A., Siegle, J. H., Denman, D. J., Bauza, M., Barbarits, B., Lee, A. K., Anastassiou, C. A., Andrei, A., Aydın, Ç., Barbic, M., Blanche, T. J., Bonin, V., Couto, J., Dutta, B., Gratiy, S. L., Gutnisky, D. A., Häusser, M., Karsh, B., … Harris, T. D. (2017). Fully integrated silicon probes for high-density recording of neural activity. *Nature*, *551*(7679), 232–236. https://doi.org/10.1038/nature24636

Kao, M. H., Doupe, A. J., & Brainard, M. S. (2005). Contributions of an avian basal ganglia–forebrain circuit to real-time modulation of song. *Nature*, *433*(7026), 638–643. https://doi.org/10.1038/nature03127

Kao, M. H., Wright, B. D., & Doupe, A. J. (2008). Neurons in a forebrain nucleus required for vocal plasticity rapidly switch between precise firing and variable bursting depending on social context. *The Journal of Neuroscience: The Official Journal of the Society for Neuroscience*, *28*(49), 13232–13247. https://doi.org/10.1523/JNEUROSCI.2250-08.2008

Kawai, R., Markman, T., Poddar, R., Ko, R., Fantana, A. L., Dhawale, A. K., Kampff, A. R., & Ölveczky, B. P. (2015). Motor Cortex Is Required for Learning but Not for Executing a Motor Skill. *Neuron*, *86*(3), 800–812. https://doi.org/10.1016/j.neuron.2015.03.024

Kobak, D., Pardo-Vazquez, J. L., Valente, M., Machens, C. K., & Renart, A. (2019). State-dependent geometry of population activity in rat auditory cortex. *eLife*, *8*. https://doi.org/10.7554/eLife.44526

Kojima, S., Kao, M. H., & Doupe, A. J. (2013). Task-related “cortical” bursting depends critically on basal ganglia input and is linked to vocal plasticity. *Proceedings of the National Academy of Sciences*, *110*(12), 4756–4761. https://doi.org/10.1073/pnas.1216308110

Kollmorgen, S., Hahnloser, R. H. R., & Mante, V. (2020). Nearest neighbours reveal fast and slow components of motor learning. *Nature*, *577*(7791), 526–530. https://doi.org/10.1038/s41586-019-1892-x

Konishi, M. (1965). The role of auditory feedback in the control of vocalization in the white-crowned sparrow. *Zeitschrift Für Tierpsychologie*, *22*(7), 770–783.

Konishi, M. (1970). Comparative neurophysiological studies of hearing and vocalizations in songbirds. *Zeitschrift Für Vergleichende Physiologie*, *66*(3), 257–272. https://doi.org/10.1007/BF00297829

Koralek, A. C., Costa, R. M., & Carmena, J. M. (2013). Temporally Precise Cell-Specific Coherence Develops in Corticostriatal Networks during Learning. *Neuron*, *79*(5), 865–872. https://doi.org/10.1016/j.neuron.2013.06.047

Kothe, C. A., & Makeig, S. (2013). BCILAB: A platform for brain-computer interface development. *Journal of Neural Engineering*, *10*(5), 056014. https://doi.org/10.1088/1741-2560/10/5/056014

Lemke, S. M., Ramanathan, D. S., Darevksy, D., Egert, D., Berke, J. D., & Ganguly, K. (2021). Coupling between motor cortex and striatum increases during sleep over long-term skill learning. *eLife*, *10*, 1–25. https://doi.org/10.7554/eLife.64303

Libourel, P.-A., Barrillot, B., Arthaud, S., Massot, B., Morel, A. L., Beuf, O., Herrel, A., & Luppi, P. H. (2018). Partial homologies between sleep states in lizards, mammals, and birds suggest a complex evolution of sleep states in amniotes. *PLoS Biology*, *16*(10), e2005982. https://doi.org/10.1371/journal.pbio.2005982

Liu, A. A., Henin, S., Abbaspoor, S., Bragin, A., Buffalo, E. A., Farrell, J. S., Foster, D. J., Frank, L. M., Gedankien, T., Gotman, J., Guidera, J. A., Hoffman, K. L., Jacobs, J., Kahana, M. J., Li, L., Liao, Z., Lin, J. J., Losonczy, A., Malach, R., … Buzsáki, G. (2022). A consensus statement on detection of hippocampal sharp wave ripples and differentiation from other fast oscillations. *Nature Communications*, *13*(1), Article 1. https://doi.org/10.1038/s41467-022-33536-x

Lorenz, C. (2024). *Song-related neuron populations in the zebra finch forebrain chronically recorded with a custom-designed Neuropixels device* [Doctoral Thesis, ETH Zurich]. https://doi.org/10.3929/ethz-b-000690541

Low, P., Shank, S. S., Sejnowski, T. J., & Margoliash, D. (2008). Mammalian-like features of sleep structure in zebra finches. *Proc Natl Acad Sci U S A*, *105*(26), 9081–9086. https://doi.org/0703452105 [pii]10.1073/pnas.0703452105

McCasland, J. S., & Konishi, M. (1981). Interaction between auditory and motor activities in an avian song control nucleus. *Proceedings of the National Academy of Sciences of the United States of America*, *78*(12), 7815–7819.

Mizrahi-Kliger, A. D., Kaplan, A., Israel, Z., & Bergman, H. (2018). Desynchronization of slow oscillations in the basal ganglia during natural sleep. *Proceedings of the National Academy of Sciences of the United States of America*, *115*(18), E4274–E4283. https://doi.org/10.1073/pnas.1720795115

Moorman, S., Ahn, J.-R., & Kao, M. H. (2021). Plasticity of stereotyped birdsong driven by chronic manipulation of cortical-basal ganglia activity. *Current Biology*, *31*(12), 2619-2632.e4. https://doi.org/10.1016/j.cub.2021.04.030

Nixdorf-Bergweiler, B. E., Bischof, H.-J., Nixdorf-Bergweiler, B. E., & Bischof, H.-J. (2007). *A Stereotaxic Atlas Of The Brain Of The Zebra Finch, Taeniopygia Guttata*. National Center for Biotechnology Information (US).

O'Keefe, J. (1976). Place units in the hippocampus of the freely moving rat. *Experimental Neurology*, *51*(1), 78–109.

Olveczky, B. P., Andalman, A. S., & Fee, M. S. (2005). Vocal experimentation in the juvenile songbird requires a basal ganglia circuit. *PLoS Biology*, *3*(5), e153. https://doi.org/10.1371/journal.pbio.0030153

Palmer, S. E., Wright, B. D., Doupe, A. J., & Kao, M. H. (2021). Variable but not random: Temporal pattern coding in a songbird brain area necessary for song modification. *Journal of Neurophysiology*, *125*(2), 540–555. https://doi.org/10.1152/jn.00034.2019

Person, A. L., Gale, S. D., Farries, M. A., & Perkel, D. J. (2008). Organization of the songbird basal ganglia, including area X. *Journal of Comparative Neurology*, *508*(5), 840–866. https://doi.org/10.1002/cne.21699

Pfenning, A. R., Hara, E., Whitney, O., Rivas, M. V., Wang, R., Roulhac, P. L., Howard, J. T., Wirthlin, M., Lovell, P. V., Ganapathy, G., Mouncastle, J., Moseley, M. A., Thompson, J. W., Soderblom, E. J., Iriki, A., Kato, M., Gilbert, M. T. P., Zhang, G., Bakken, T., … Jarvis, E. D. (2014). Convergent transcriptional specializations in the brains of humans and song-learning birds. *Science*, *346*(6215). https://doi.org/10.1126/science.1256846

Prerau, M. J., Brown, R. E., Bianchi, M. T., Ellenbogen, J. M., & Purdon, P. L. (2017). Sleep Neurophysiological Dynamics Through the Lens of Multitaper Spectral Analysis. *Physiology (Bethesda, Md.)*, *32*(1), 60–92. https://doi.org/10.1152/physiol.00062.2015

Santos, F. J., Oliveira, R. F., Jin, X., & Costa, R. M. (2015). Corticostriatal dynamics encode the refinement of specific behavioral variability during skill learning. *eLife*, *4*, e09423. https://doi.org/10.7554/eLife.09423

Scharff, C., & Nottebohm, F. N. (1991). A comparative study of the behavioral deficits following lesions of various parts of the zebra finch song system: Implications for vocal learning. *The Journal of Neuroscience: The Official Journal of the Society for Neuroscience*, *11*(9), 2896–2913.

Schneider, M., Broggini, A. C., Dann, B., Tzanou, A., Uran, C., Sheshadri, S., Scherberger, H., & Vinck, M. (2021). A mechanism for inter-areal coherence through communication based on connectivity and oscillatory power. *Neuron*, *109*(24), 4050-4067.e12. https://doi.org/10.1016/j.neuron.2021.09.037

Shein-Idelson, M., Ondracek, J. M., Liaw, H., Reiter, S., & Laurent, G. (2016). Slow waves, sharp waves, ripples, and REM in sleeping dragons. *Science (New York, N.Y.)*, *352*(6285), 590–595. https://doi.org/10.1126/science.aaf3621

Solis, M. M., Brainard, M. S., Hessler, N. A., & Doupe, A. J. (2000). Song selectivity and sensorimotor signals in vocal learning and production. *Proceedings of the National Academy of Sciences of the United States of America*, *97*(22), 11836–11842. https://doi.org/10.1073/pnas.97.22.11836

Stepanek, L., & Doupe, A. J. (2010). Activity in a cortical-basal ganglia circuit for song is required for social context-dependent vocal variability. *Journal of Neurophysiology*, *104*(5), 2474–2486. https://doi.org/10.1152/jn.00977.2009

Tachibana, R. O., Lee, D., Kai, K., & Kojima, S. (2022). Performance-Dependent Consolidation of Learned Vocal Changes in Adult Songbirds. *Journal of*

Neuroscience, *42*(10), 1974–1986. https://doi.org/10.1523/JNEUROSCI.1942-21.2021

Tian, L. Y., Warren, T. L., Mehaffey, W. H., & Brainard, M. S. (2023). Dynamic top-down biasing implements rapid adaptive changes to individual movements. *eLife*, *12*, e83223. https://doi.org/10.7554/eLife.83223

Tumer, E. C., & Brainard, M. S. (2007). Performance variability enables adaptive plasticity of "crystallized" adult birdsong. *Nature*, *450*(7173), 1240–1244. https://doi.org/10.1038/nature06390

Vates, G. E., & Nottebohm, F. (1995). Feedback circuitry within a song-learning pathway. *Proceedings of the National Academy of Sciences of the United States of America*, *92*(11), 5139–5143.

Vates, G. E., Vicario, D. S., & Nottebohm, F. (1997). Reafferent thalamo- "cortical" loops in the song system of oscine songbirds. *The Journal of Comparative Neurology*, *380*(2), 275–290.

Warren, T. L., Tumer, E. C., Charlesworth, J. D., & Brainard, M. S. (2011). Mechanisms and time course of vocal learning and consolidation in the adult songbird. *Journal of Neurophysiology*, *106*(4), 1806–1821. https://doi.org/10.1152/jn.00311.2011

Woolley, S. C., & Kao, M. H. (2015). Variability in action: Contributions of a songbird cortical-basal ganglia circuit to vocal motor learning and control. *Neuroscience*, *296*, 39–47. https://doi.org/10.1016/j.neuroscience.2014.10.010

Yanagihara, S. Y., & Hessler, N. A. (2012). Phasic basal ganglia activity associated with high-gamma oscillation during sleep in a songbird. *Journal of Neurophysiology*, *107*(1), 424–432. https://doi.org/10.1152/jn.00790.2011

Yeganegi, H., Luksch, H., & Ondracek, J. M. (2019). Hippocampal-like network dynamics underlie avian sharp wave-ripples. *bioRxiv*, 825075. https://doi.org/10.1101/825075

Yeganegi, H., & Ondracek, J. M. (2023). Multi-channel recordings reveal age-related differences in the sleep of juvenile and adult zebra finches. *Scientific Reports*, *13*(1), Article 1. https://doi.org/10.1038/s41598-023-35160-1

Yeganegi, H., & Ondracek, J. M. (2025). Local sleep in songbirds: Different simultaneous sleep states across the avian pallium. *Journal of Sleep Research*, *34*(3), e14344. https://doi.org/10.1111/jsr.14344

Zai, A. T., Cavé-Lopez, S., Rolland, M., Giret, N., & Hahnloser, R. H. R. (2020). Sensory substitution reveals a manipulation bias. *Nature Communications*, *11*(1), 5940. https://doi.org/10.1038/s41467-020-19686-w

968 # Figures and Table Legends

969

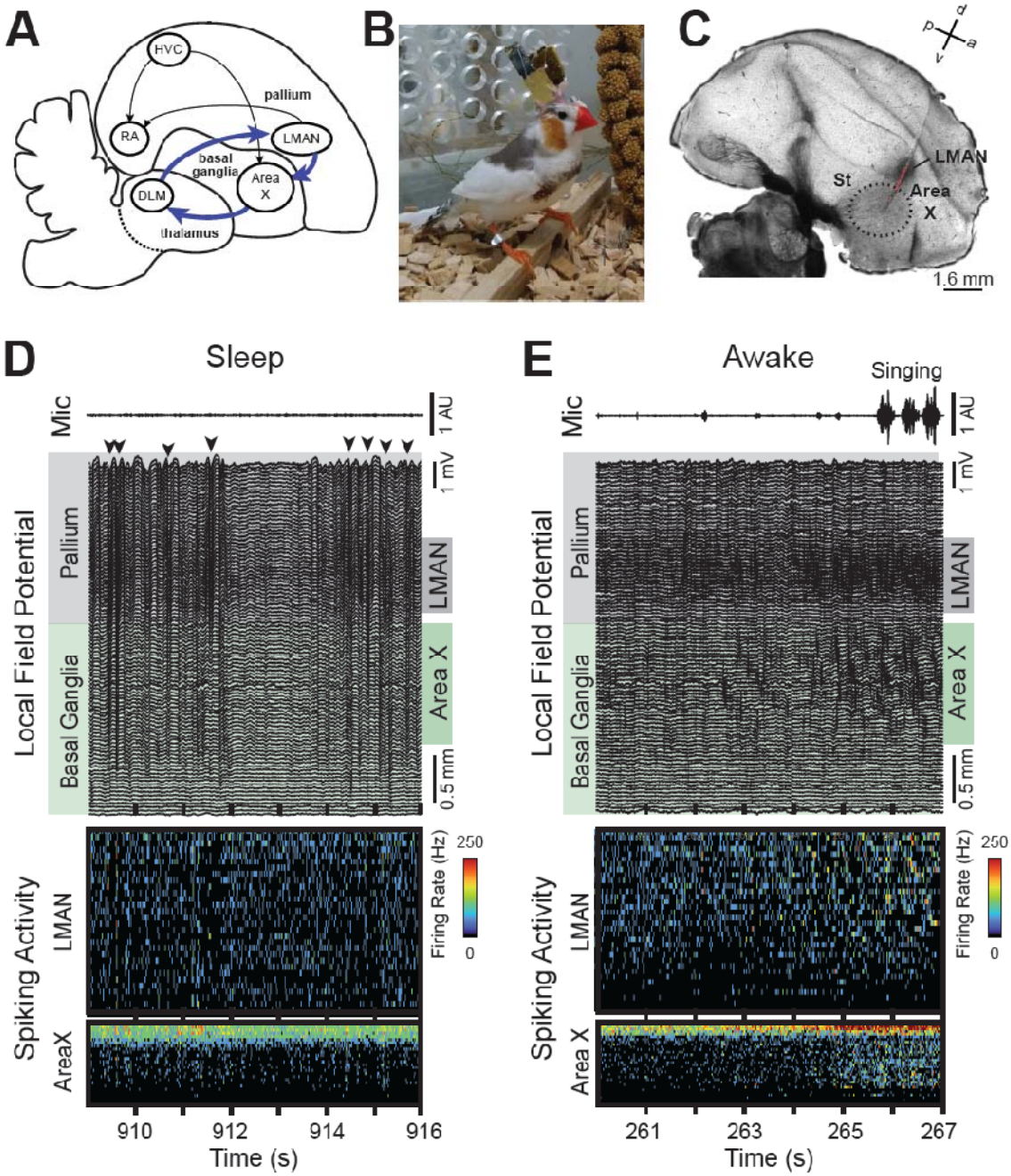

970

971

972 **Figure 1: Pallial-basal ganglia dynamics during sleep and awake behavior in a**

973 **songbird. (A)** Schematic depicts the basal ganglia-thalamocortical circuit (blue arrows).

974 Black arrows indicate other important connections of the song system. HVC, proper name;

975 RA, robust nucleus of the arcopallium; LMAN, lateral magnocellular nucleus of the

nidopallium; Area X, proper name; DLM, medial dorsolateral nucleus of the thalamus. **(B)** Image of a male zebra finch implanted with a Neuropixels1.0 probe. **(C)** Histological brain slice depicting the Neuropixels electrode track (red DiI fluorescence). Area X is indicated with a dotted black line. St, striatum; d, dorsal; a, anterior; v, ventral; p, posterior; for other abbreviations, see (A). Histology from ZF-2, cut at room temperature on a vibratome. **(D)** 7 s segment of the bandpass-filtered (0.5-250Hz) local field potentials (LFP) recorded during putative sleep in subadult ZF-1 and corresponding microphone signal (top, arbitrary units (AU)). Black arrowheads (LFP, top) indicate large amplitude negative LFP deflections. Recording sites were located in the pallium (gray shading) and basal ganglia (green shading) and are organized according to depth. Dark gray box (LMAN, right side) indicates LFPs that correspond to LMAN; dark green box (Area X, right side) indicates LFPs that correspond to Area X. Below, corresponding spiking activity for identified LMAN or Area X neurons. Firing rate is indicated with the color scale, and neurons are sorted according to firing rate. Note how neural activity transitions from sparse and synchronous firing aligned to the LFP troughs to asynchronous firing at 912-914 s. **(E)** 7 s segment of the bandpass-filtered LFP recorded during active daytime behavior in ZF-1. Figure conventions same as in (D). Note the calling and singing behavior recorded on the microphone signal (top) and the corresponding activity in LMAN and Area X. Note also the absence of large amplitude negative deflections in the LFP as observed during putative sleep.

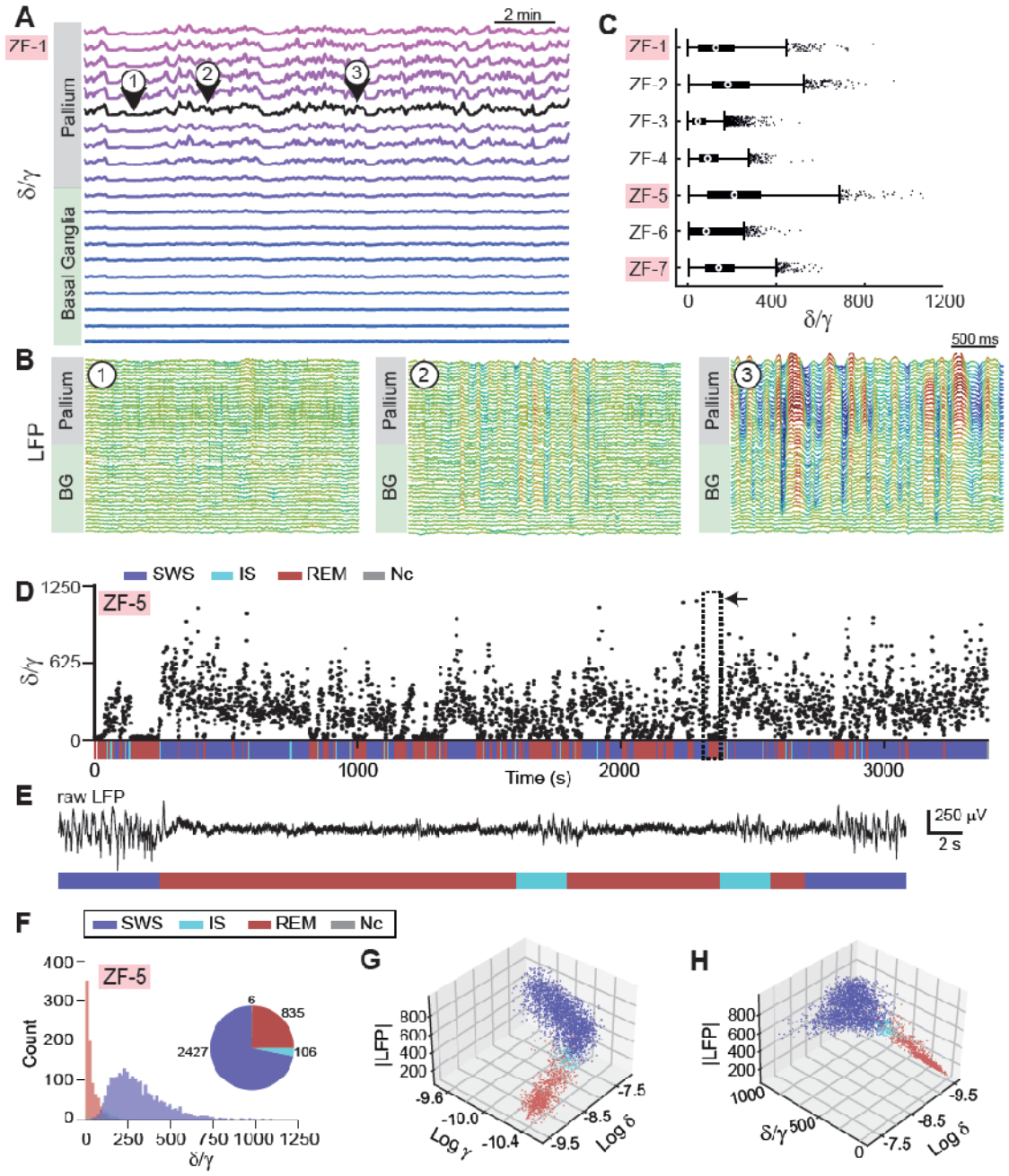

Figure 2: Identification of sleep stages and representative neural dynamics. (A) Ratio of δ/γ power for consecutive depths along the Neuropixels shank. Each trace is separated by 200 um. Black trace indicates the δ/γ trace calculated for a centrally located pallial (LMAN) LFP. Numbers and arrows indicate low (1), middle (2), and high (3) δ/γ values. δ/γ values calculated for a 3-s LFP window, as depicted in (B). Data from sub-adult ZF-1 (pink shading). **(B)** 3-second segments of local field potential (LFP) activity from pallial and BG

sites for the low, middle, and high δ/γ values indicated in (A). Each trace is separated by 80 um. Note the large amplitude slow wave dynamics present for high δ/γ values indicated in (3). Linear color scale for visualization purposes only. Data from sub-adult ZF-1. **(C)** Box plots indicate average δ/γ values calculated in 3-s windows from a centrally located LMAN channel for the duration of the sleep phase per bird. The left and right edges of the box represent the 25th and 75th percentile, respectively, and the middle dot represents the median. Whiskers extends to the most extreme datapoints not considered outliers, and datapoints beyond this range are indicated as dots. Sub-adult animals are indicated with pink shading of their names. **(D)** δ/γ values for an entire recording duration for an example bird (sub-adult ZF-5) plotted with the identified sleep stages as colored bars below. SWS, slow wave sleep; IS, intermediate sleep; REM, rapid eye-movement sleep; Nc, not categorized. Dotted black box indicated with the black arrow is enlarged in (E). **(E)** 50 s trace of raw LFP from the LMAN channel used for sleep staging (see Methods for details). Color-coded bars indicate classified sleep stages. Note how SWS segments correspond to a large amplitude LFP signal and REM segments correspond to a low amplitude LFP signal. **(F)** Histogram of δ/γ values grouped according to identified sleep states together with the proportions of sleep stages depicted in a pie chart for the bird in (D). Note how SWS segments correspond to high δ/γ values and REM segments correspond to low δ/γ values. **(G, H)** Plots show that sleep state clusters are segregated in 3-D space according to the features used for classification, e.g., mean LFP magnitude, the delta (δ) and gamma (γ) power, δ/γ values. Each dot represents a 1-s snippet of sleeping data (resolution of the automated sleep staging procedure). Same bird as in (D-F).

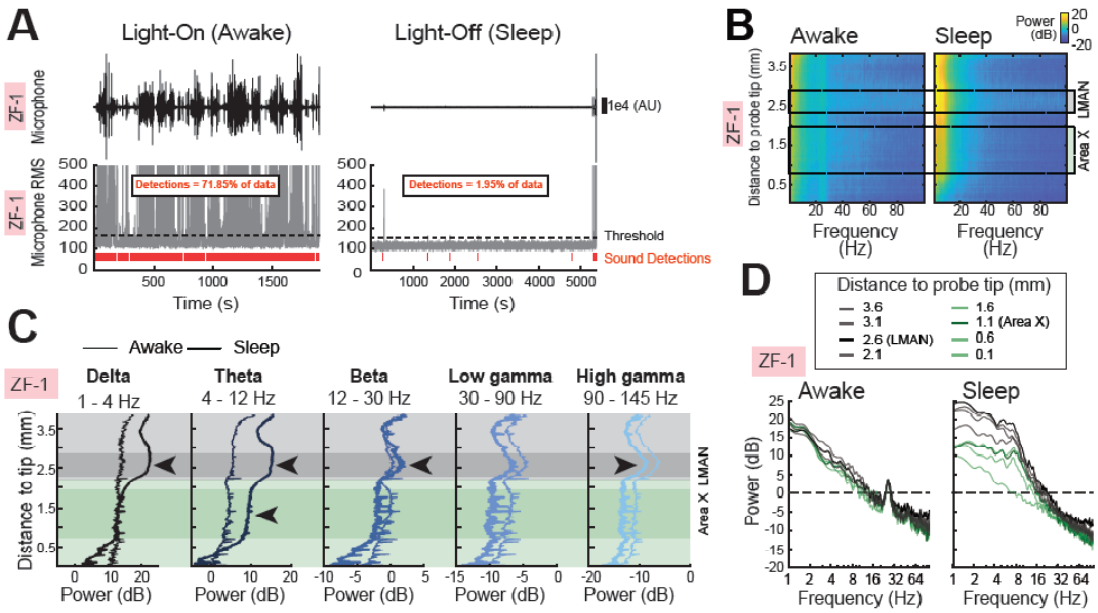

Figure 3: Sleep-related modulation of low-frequency power is higher in pallium compared to the striatum (A) Comparison of microphone signals recorded during the light on (awake) period and the light off (sleep) period. Top traces (black) indicate the raw microphone signal; scale is the same across recordings (arbitrary units, AU). Bottom traces (gray) indicate the root mean square (RMS) of the microphone signal. Black dotted line indicates the manually set threshold, and threshold crossings indicate sound detections (red lines). The overall percent of data for which sounds were detected is stated (top). Recording from sub-adult ZF-1. Microphone data from other birds can be found in Supplementary Fig. 3-1. **(B)** The color-coded power spectrum density (PSD) of the LFP signal for each electrode is displayed, organized by depth (dorsal to ventral), for both the awake state (left) and sleep state (right) for sub-adult ZF-1. Warm color indicates high power; cool colors indicate low power. The electrode depths corresponding to LMAN (gray box, dashed line) and Area X (green box, dashed line) are indicated. The analysis is based on the average PSD derived from 10 randomly selected 10-sec windows. **(C)** Power distribution across electrode sites provide a detailed comparison between awake (thin lines) and sleep (thick lines) for different frequency bands. LMAN exhibits higher gamma band power (90-145 Hz) during awake states compared to sleep states (LMAN; black arrowheads). In contrast LMAN exhibits

1044 higher power in low frequency bands (1-30 Hz) during sleep compared to awake states
1045 (LMAN; black arrowheads). A difference in sleep and awake states in Area X is largely
1046 absent, with the exception of the theta band power (4-12 Hz), which showed a slight
1047 increase in two birds during sleep (Area X; black arrowhead). **(D)** The marginal distribution of
1048 power across depths is displayed for awake and sleep states for each bird. Note that the
1049 distances in the legend refer to the distance from the probe tip, (i.e., 3.6 mm from the probe
1050 tip). The black line indicates depth associated with LMAN (i.e., 2.6 mm); note how it is
1051 strongly modulated by sleep. Gray lines indicate other depths associated with the pallium.
1052 The dark green line indicates the depth associated with Area X; light green lines indicate
1053 other depths associated with the BG. Dotted line indicates 0 dB. Spectral data for other birds
1054 are depicted in Supplementary Fig. 3-2

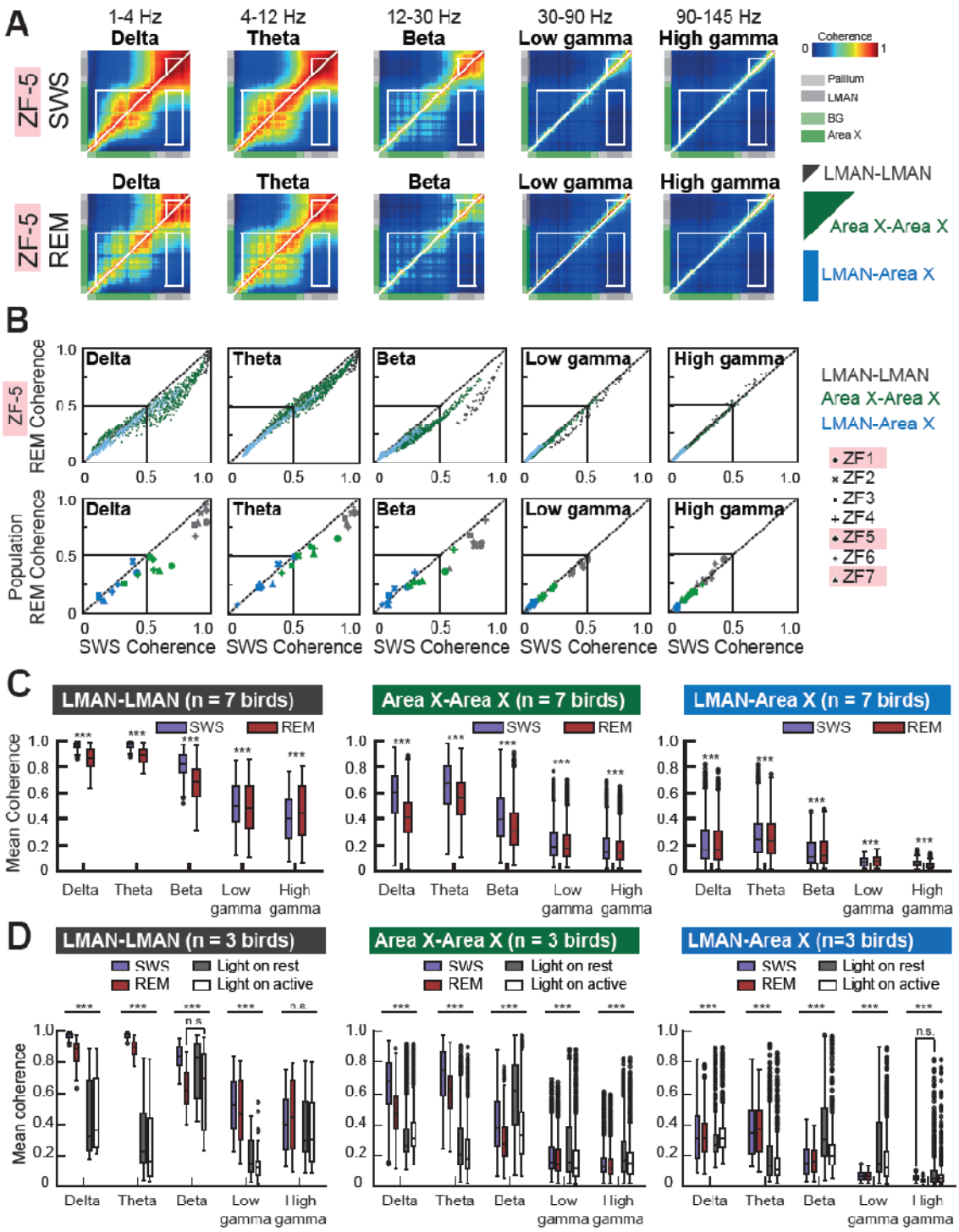

Figure 4: LFP coherence in the pallial-striatal circuit is modulated by behavioral states. (A) Heat maps represents a color-coded representation of the average pairwise coherence calculated for all passbands for all SWS segments (top) and REM sleep segments (bottom). Warm colors indicate high coherence values, and cool colors indicate

1060 low coherence values. The diagonal white line indicates symmetry. The white triangles along
1061 the line of symmetry indicate the pallial electrode sites that were included in the LMAN-
1062 LMAN coherency analysis (corresponding to the gray LMAN shading; small black triangle,
1063 right side) or the BG electrode sites that were included in the Area X-Area X coherence
1064 analysis (green Area X shading; large dark green triangle, right side). The white rectangle
1065 (lower right quadrant) indicates the sites that were included in the LMAN-Area X coherency
1066 analysis (blue rectangle, right side). Data from sub-adult ZF-5. **(B)** Scatter plots (top row)
1067 depict the average REM sleep versus SWS coherence value for each electrode pair plotted
1068 for different frequency bands in each panel for sub-adult ZF-5. LMAN-LMAN comparisons
1069 (gray dots); Area X- Area X comparisons (green dots) and LMAN-Area X comparisons (blue
1070 dots). Black lines at 0.5 for visualization purposes only. Bottom row depicts the mean
1071 coherence values for all 7 birds (symbols); colors indicate the coherence comparisons (e.g.,
1072 LMAN-LMAN in dark gray). Subadult birds are indicated with pink shading of their names.
1073 **(C)** Comparison between REM and SWS coherences for different passbands. Box plots
1074 indicate the median coherency values across different frequency bands for within-LMAN
1075 comparisons (left panel), within-Area X comparisons (middle panel) and LMAN-Area X
1076 comparisons (right panels). Blue boxes indicate SWS, red boxes indicate REM sleep. The
1077 box bottom and top edges represent the 25th and 75th percentile, respectively, and the
1078 middle line represents the median. Whiskers extends to the most extreme datapoints not
1079 considered outliers, and datapoints beyond this range are indicated as circles. Asterisks
1080 indicate significance (Wilcoxon sign rank test; ***$p \leq 0.001$). **(D)** Comparison between
1081 awake and sleep coherences for different passbands for 3 birds. SWS (blue box); REM
1082 sleep (red box); Light on rest (gray box) Light on active (white box). Delta and theta band
1083 coherences were significantly lower during the awake states compared to the sleep states
1084 for all channel comparisons. Figure conventions same as in (C). Asterisks indicate
1085 significance (Friedman test for multiple comparisons; ***$p \leq 0.001$). The non-significant
1086 comparisons from the post-hoc Nemeyni test are marked in the figure (n.s). All other
1087 pairwise comparisons were significant with the post-hoc test.

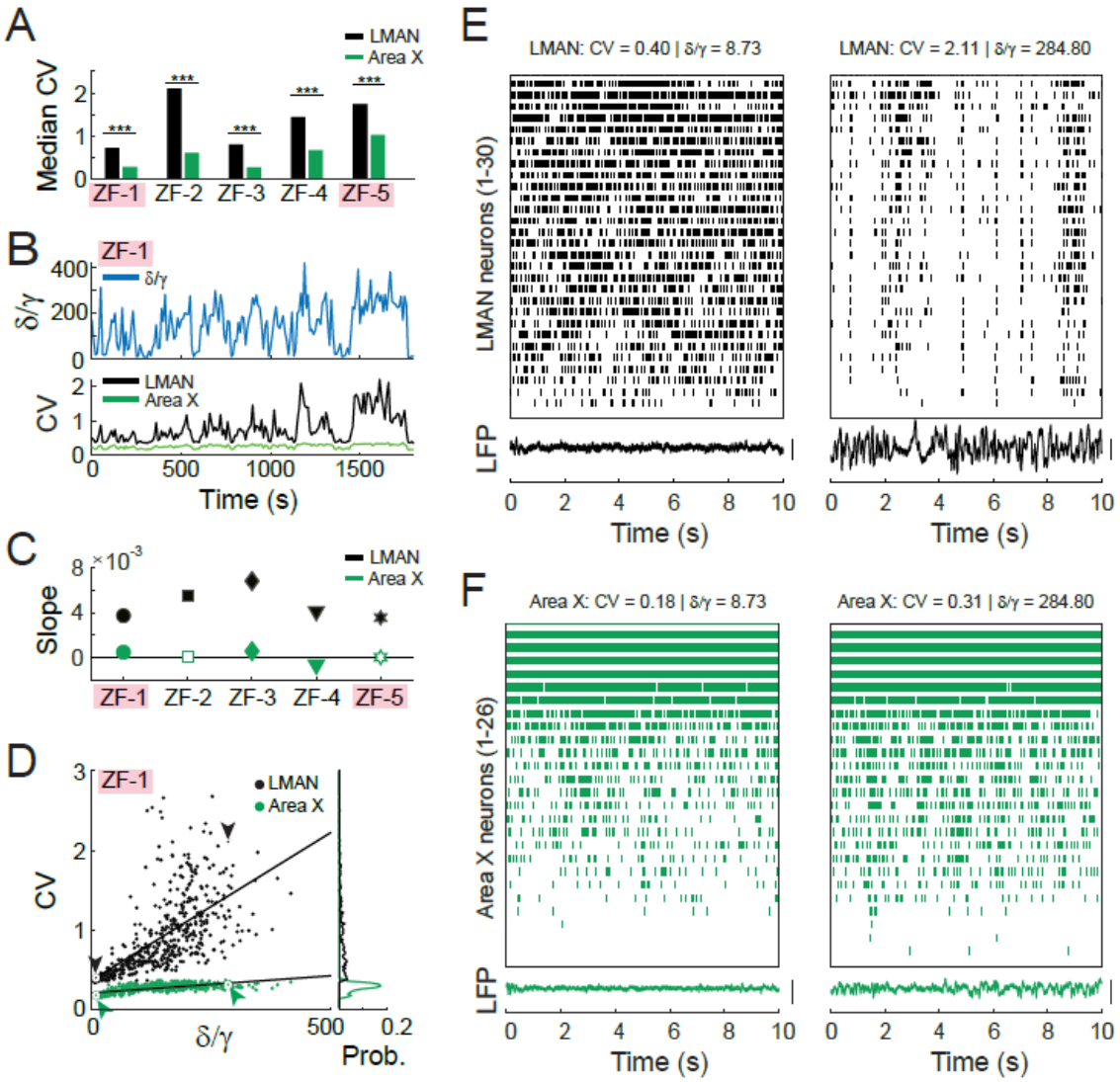

Figure 5: Spiking variability is significantly higher for LMAN neurons compared to Area X neurons. (A) Bar plots summarize CV values for 7 finches (black bars, LMAN population; green bar, Area X population). CV values were higher for LMAN populations compared to Area X populations. Sub-adult birds are indicated by pink shading of their names. **(B)** δ/γ values (top, blue line) were highly correlated with CV values (bottom) for both LMAN and Area X populations. δ/γ values and CV values computed in 10 s windows. **(C)** The slope of regression fits between CV and δ/γ was consistently higher in LMAN compared to Area X across birds. Filled symbols indicate significant correlations ($p < 0.01$). **(D)** Scatter plot indicates the CV versus δ/γ values for ZF-1. LMAN, black dots; Area X, green dots. Black and green arrows indicate the data points that correspond to the 10 s snippet of data

plotted in (D) and (E). The marginal distributions for the CV values are plotted (right) for LMAN (black line) and Area X neurons (green line). **(E)** Spiking raster plot for 33 LMAN neurons for an example time window with low CV value (left plot) and a high CV value (right box). Each tick corresponds to a spike and neurons are sorted by their average spiking activity from high (top) to low (bottom). Corresponding 10 s LFP trace is plotted at the bottom of the raster plot. Vertical bar is 500 uV. Data correspond to black arrows in (D). **(F)** Spiking raster plot for 27 Area X neurons for a low CV value (left plot) and a high CV value (right box). Figure convention same as in (E). Data correspond to green arrows in (D). Vertical bar is 500 uV.

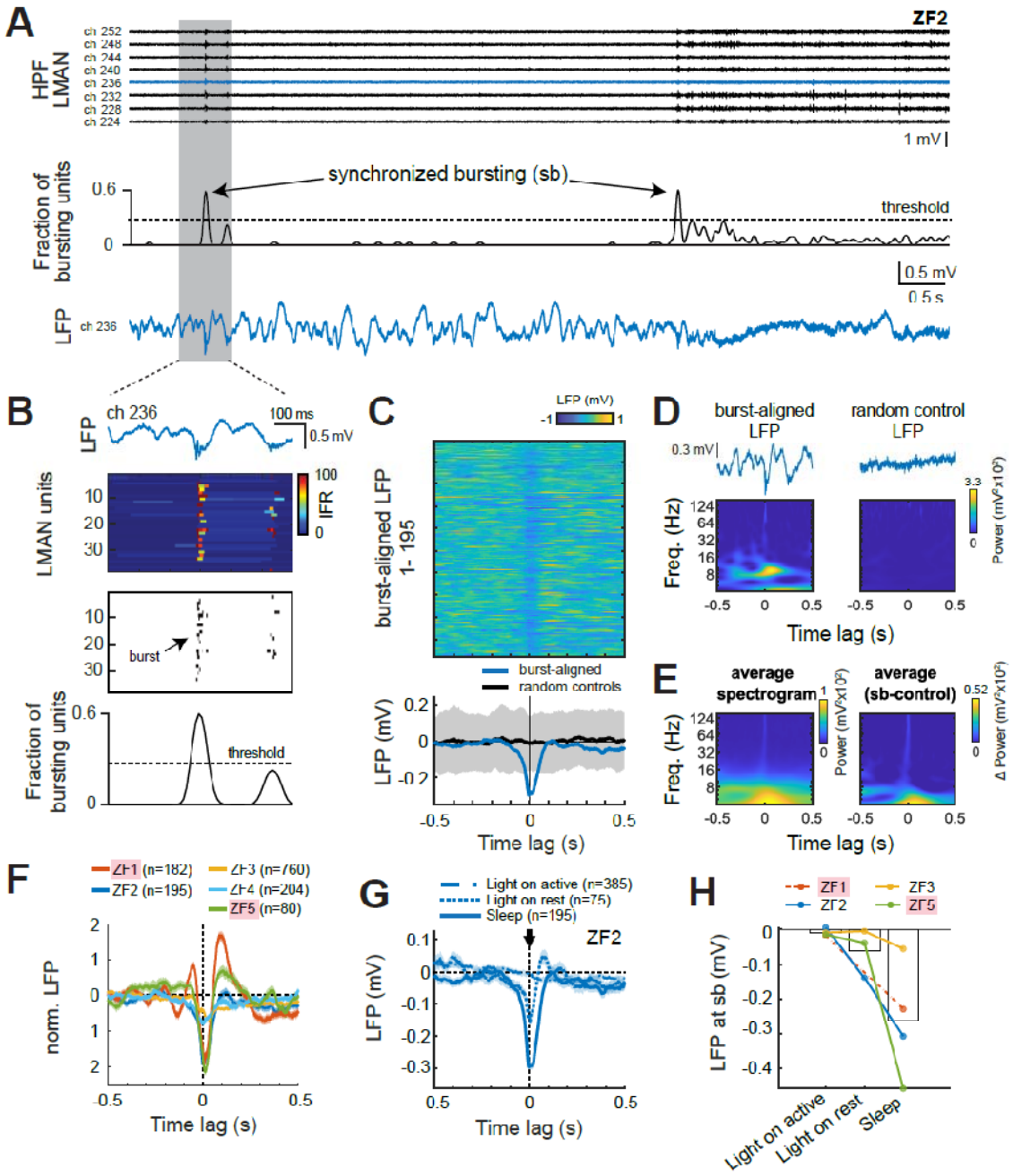

Figure 6: Synchronized bursting in LMAN is associated with a negative deflection in the LFP (A) Two examples of synchronized bursting activity in LMAN from ZF-2. Top panel depicts high-pass filtered (HPF) electrode signals from eight electrodes in LMAN. Middle panel depicts the detection of synchronized bursting (black line) based on the smoothed fraction of bursting units in a 50 ms window exceeding the 99.5th percentile threshold. Bottom panel depicts the raw LFP (blue, same electrode as in top panel). Area indicated by

gray shading is expanded in (B). **(B)** Zoom-in on the highlighted gray window in (A). Top panel depicts the instantaneous firing rate (IFR) of all LMAN units (n = 32), color-coded and clipped at 100 Hz. The panel below depicts the occurrence of bursts in black for each LMAN unit. Lower panels same as in (A). **(C)** Upper panel depicts 195 bursting-aligned LFP segments detected from ch 236, stacked and color-coded. Events are sorted by the total fraction of bursting units. Lower panel indicates the average bursting-aligned LFP (blue) and the same statistics for randomly selected LFP segments (black, gray shading is +/- SD). **(D)** Two raw LFP snippets (top panel) and their corresponding scalograms (bottom panel). The left example shows a bursting aligned LFP. The right depicts random control (right). **(E)** The average bursting aligned-LFP scalogram (left) and its difference to the average random control scalogram (right). Note how the power density for the synchronized burst is highly elevated at low frequencies. Sb, synchronized burst. **(F)** LFPs show consistent negative dip during a synchronized burst. Each line indicates the bursting-aligned LFP normalized to the random control (z-norm ± SEM) for each bird. **(G)** The average burst-aligned LFP ± SEM across different states for ZF-2. Note that the LFP dip remains visible during light-on resting periods (short-dashed line), though it is reduced in magnitude, and becomes further diminished during light-on active periods (long-dashed line). **(H)** Comparison of LFP dips across all birds with available awake data shows that the strongest deflections occur during light-off periods. No bursting events were detected for ZF-1 during light-on active periods. See Supplementary Fig. 6-1 for more details.

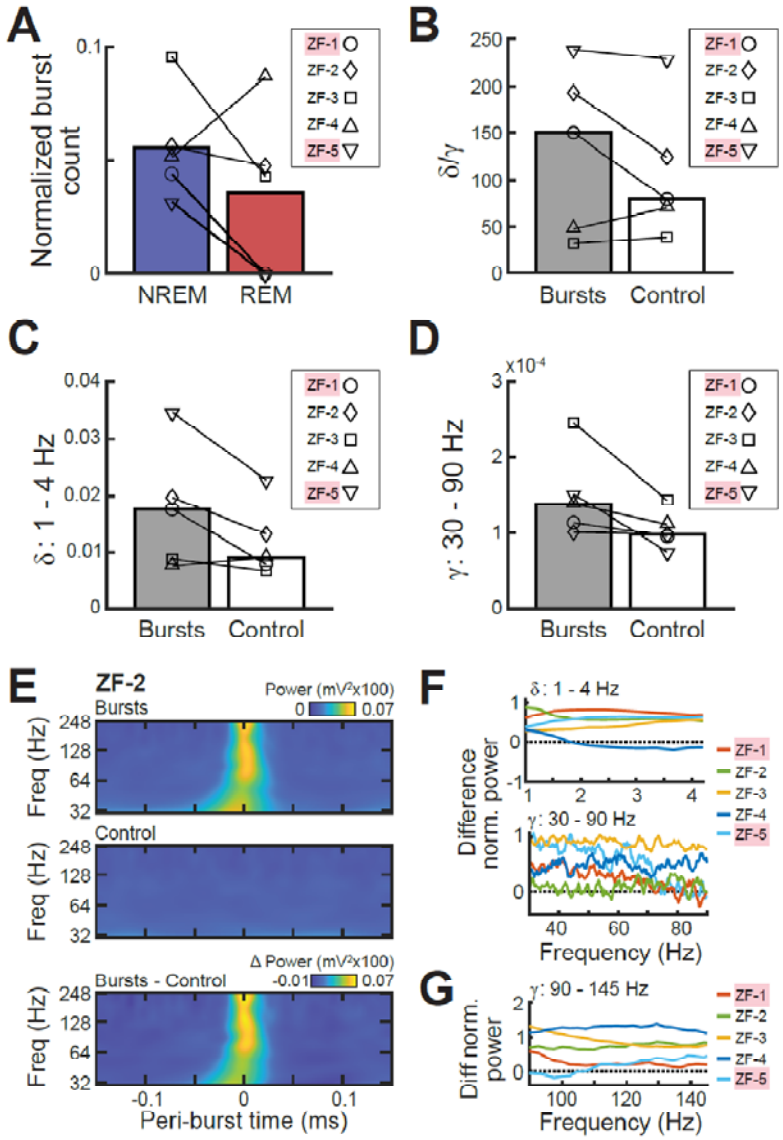

Figure 7: Synchronized bursts occur during NREM sleep and are associated with higher γ activity. (A) Bar plots indicate median number of bursts associated with each sleep state normalized by the overall sleep state duration in seconds across birds (see Fig. 2F, G). With the exception of ZF-4, most birds showed more bursts detected during NREM states compared to REM sleep states. NREM states included both SWS and IS classified states. Symbols indicate median data for each bird. Sub-adults are indicated with pink shading of their names. **(B)** Bar plots indicate median δ/γ value calculated for 500 ms segments of LFP that were centered on a synchronized burst detection (Bursts, grey bar) compared to the mean value of 500 ms control segments of LFP that were temporally shifted

away from the burst detection by a random offset (Control, white bar; see Methods for details). Symbols indicate median data for each bird. Note how δ/γ values are on average higher for the control LFP segments. **(C)** Same convention as in (B) for δ values. Note how δ values are higher for the burst LFP segments compared to the control LFP segments. **(D)** Same convention as in (B) and (C) for γ values. Note the higher γ values during the burst LFP segments compared to the control LFP segments. **(E)** Spectrograms display the average peri-burst time window surrounding a burst event (top), a control event (middle), and the difference in power between the burst event and the control event (bottom) for ZF-2. Note the increase in power surrounding the burst event that extends up into the high γ range. **(F)** Panels display the normalized PSD for different frequency ranges: δ (1-4 Hz, top), low γ (30-90 Hz, middle), and high γ (90-145 Hz, bottom plot). Normalized PSD indicates the difference between the burst events and the control events divided by the standard deviation of the control events. Different line colors indicate different birds. Note how data for all birds fall above the zero (dotted line) indicating higher values during the burst event compared to control events.

ZF	Animal ID	Age (dph)	Rec location	Start of recording	Data available	# LMAN units	# Area X units	Histology
1	g4r4	84	Paris	03:58 pm*	LFP+SU	30	26	Vibratome
2	r15v15	125	Paris	8:42 pm	LFP+SU	32	6	Vibratome
3	j8v8	124	Paris	05:18 am	LFP+SU	40	19	Missing**
4	Redred	177	Bordeaux	05:30 am	LFP+SU	28	7	Cryostat
5	r5n5	85	Paris	5:21 pm*	LFP+SU	6	3	Vibratome
6	black/cyan	232	Bordeaux	04:17 am	LFP	-	-	Cryostat
7	no_label	76	Bordeaux	00:28 am	LFP	-	-	Missing**

Table 1: Information related to experimental animals

Age refers to the age at the recording time in days post hatch (dph).

For all birds recorded in Bordeaux, data were recorded continuously throughout the night, and a 1-hour time period was selected for the analysis in this paper. The times indicated in the “Start of Recording” column indicates the start of the 1-hour recording time for those birds.

* For some Paris birds, the dark period (lights off) time was initiated earlier than normal and recording sessions started in the late afternoon (in the dark).

LFP, local field potential
SU, spiking unit (including single and multi-unit activity from high-pass filtered voltage traces)

** These animals died during the Covid laboratory lock-down in 2020 and it was not possible to retrieve the brains in time to perform histology. Electrode reconstruction was then based on response mapping of the brain areas that was performed during the probe implantation, as well as by visualizing the sorted spiking data for LMAN and Area X, which was distinguishable on the basis of spike amplitude and rate.

Brain Area	Frequency range	SWS: Median coherence (Min, Max values)	REM: Median coherence (Min, Max values)	Wilcoxon signed rank test (p value)
LMAN	**Delta**: 1 – 4 Hz	**0.942** (0.693, 0.996)	**0.828** (0.307, 0.987)	7.94E-75
	Theta: 4 – 12 Hz	**0.944** (0.741, 0.995)	**0.838** (0.479, 0.986)	4.11E-76
	Beta: 12 – 30 Hz	**0.751** (0.191, 0.961)	**0.608** (0.191, 0.961)	6.00E-76
	Low gamma: 30 – 90 Hz	**0.345** (0.056, 0.848)	**0.309** (0.052, 0.860)	2.73E-35
	High gamma: 90 – 140 Hz	**0.230** (0.028, 0.764)	**0.222** (0.022, 0.806)	0.134
Area X	**Delta**: 1 – 4 Hz	**0.561** (0.006, 0.955)	**0.366** (0.006, 0.876)	0
	Theta: 4 – 12 Hz	**0.649** (0.044, 0.981)	**0.516** (0.055, 0.935)	0
	Beta: 12 – 30 Hz	**0.371** (0.026, 0.909)	**0.264** (0.020, 0.909)	0
	Low gamma: 30 – 90 Hz	**0.174** (0.022, 0.767)	**0.162** (0.0197, 0.699)	6.69E-292
	High gamma: 90 – 140 Hz	**0.132** (0.021, 0.703)	**0.128** (0.0178, 0.649)	1.12E-97
LMAN - X	**Delta**: 1 – 4 Hz	**0.172** (0.001, 0.924)	**0.177** (0.003, 0.846)	4.64E-16
	Theta: 4 – 12 Hz	**0.295** (0.011, 0.919)	**0.254** (0.010, 0.823)	9.10E-69
	Beta: 12 – 30 Hz	**0.129** (0.006, 0.615)	**0.120** (0.005, 0.607)	2.80E-04
	Low gamma: 30 – 90 Hz	**0.074** (0.013, 0.274)	**0.076** (0.014, 0.272)	0.325
	High gamma: 90 – 140 Hz	**0.059** (0.016, 0.248)	**0.045** (0.012, 0.207)	1.83E-306

Table 2: Average coherence values for all birds (n = 7) used for analysis in Figure 4.

Bird	LMAN CV median (min, max)	Area X CV median (min, max)	Wilcoxon ranksum test (p Value)
ZF-1	0.73 (0.33-2.68)	0.28 (0.14-0.37)	1.08E-174
ZF-2	2.14 (0.32-5.16)	0.62 (0.39-0.99)	1.74E-73
ZF-3	0.80 (0.39 -6.42)	0.27 (0.16-0.54)	6.71E-318
ZF-4	1.44 (0.44-5.44)	0.67 (0.43-0.98)	3.94E-56
ZF-5	1.62 (0.88-5.08)	1.04 (0.86-1.22)	3.00E-75
Population median	1.44	0.62	

Table 3: Median CV values were significantly higher for LMAN neurons compared to Area X neurons. Median values and range. Population statistics are computed across median CVs. p value is the result of a Wilcoxon rank sum test.

Bird	LMAN: CV versus δ/γ			Area X: CV versus δ/γ	
	R	p		R	p
ZF-1	0.67	7.58E-71		0.73	2.45E-88
ZF-2	0.43	2.08E-15		0.05	0.42
ZF-3	0.32	1.17E-25		0.24	2.06E-14
ZF-4	0.16	0.0034		-0.28	3.65E-07
ZF-5	0.71	5.40E-63		-0.09	0.085

Table 4: LMAN CV values were significantly and positively correlated with δ/γ values for 5/5 zebra finches. Correlations for Area X neurons were more heterogeneous. R, Pearson correlation coefficient.